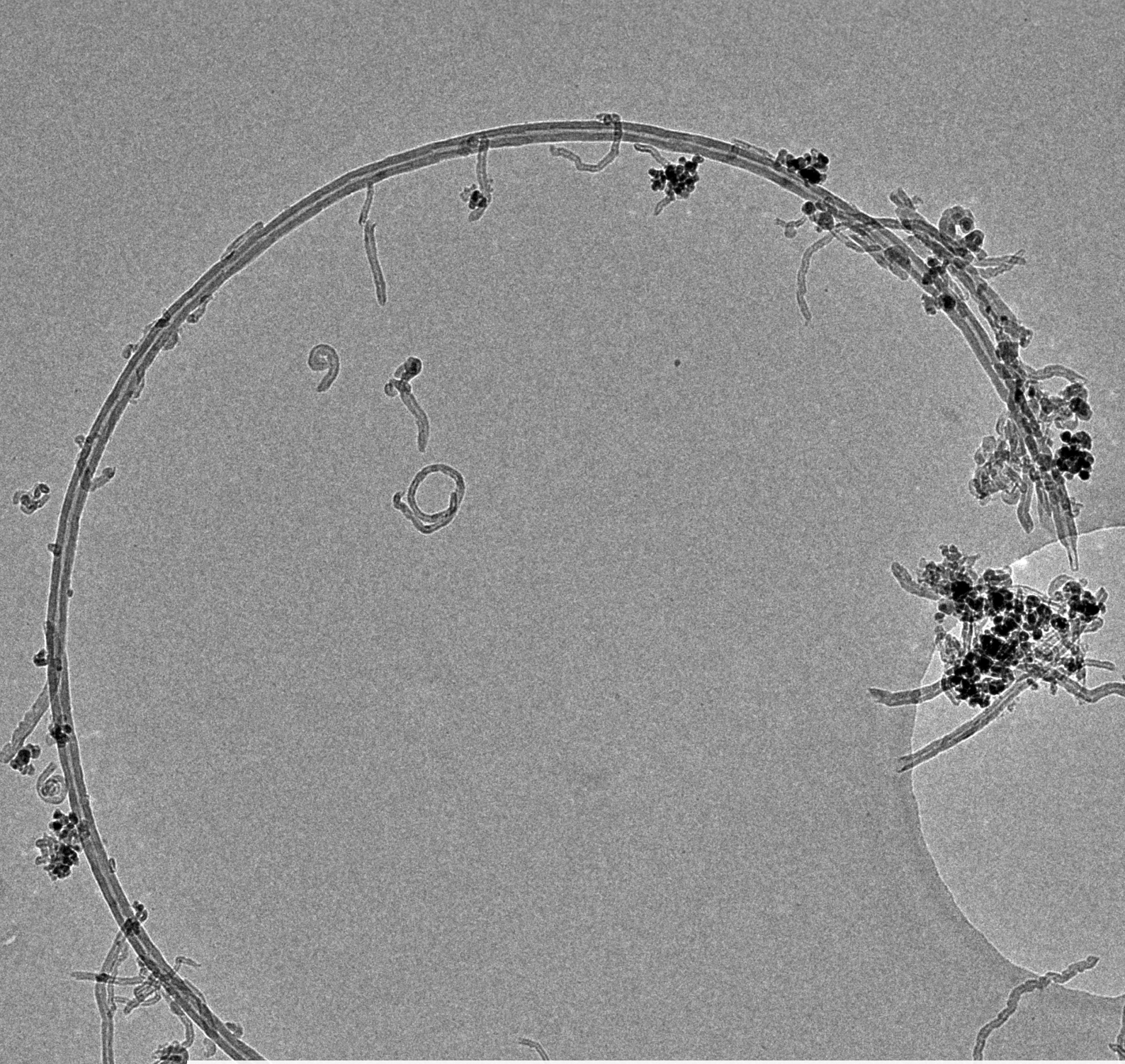

Deactivation Mechanism for Ni-based Dry Reforming Catalysts

Theodora-Alexia Asimakidis | Master Thesis | 2024
Engineering Nanoscience | Lund University

Deactivation Mechanism for Ni-based Dry Reforming Catalysts

by

Theodora-Alexia Asimakidis

Centre for Analysis and Synthesis | Lund University (LU)

Technical University of Denmark (DTU)

Spring 2024

Supervisor (LU): Prof. Reine Wallenberg
Co-Supervisor (DTU): Prof. Thomas Willum Hansen
Examiner (LU): Prof. Jan-Olle Malm

Postal Address
P.O. Box 124
SE-221 00 Lund, Sweden

Visiting Address
Naturvetarevägen 14

Telephone
+46 46 222 00 00

Abstract

Dry reforming of methane (DRM) is a promising method for carbon dioxide utilization and hydrogen production, converting CO_2 and CH_4 into syngas (H_2 and CO) using catalysts. Despite its potential, industrial implementation has yet to prevail due to challenges in loss of activity of the catalyst. Carbon deposition (coking) and catalyst particle agglomeration (sintering) occurring during the DRM reaction lead to loss in catalyst activity, thereby lowering hydrogen production yield [1, 7]. This thesis aims to determine whether the addition of alkali promoters on Ni catalysts supported on yttria stabilised zirconia (YSZ) reduces coking and sintering, and whether the catalytic performance and stability is enhanced.

Four samples were analysed: pre and post DRM reaction, with and without promoters, focusing on the comparison between the post reaction samples. Transmission electron microscopy (TEM) imaging was used to examine the various carbon structures formed from coking. Scanning transmission electron microscopy with energy-dispersive X-ray spectroscopy (STEM-XEDS) mapped the Ni catalyst size distribution to examine sintering. Temperature programmed oxidation (TPO) and catalyst activity measurements were used to examine coking levels and catalytic performance.

The post reaction sample, Ni/YSZ with added alkali promoters, revealed significantly less coking than the post reaction unpromoted Ni/YSZ sample. Sintering levels were comparable in both of the post reaction samples, with an average particle size of 18.8 nm for the alkali promoted sample and 21.8 nm for the unpromoted sample. The alkali promoted sample exhibited a 10% decrease in catalytic activity compared to 20% for the unpromoted sample over a 50-hour reaction period. These findings indicate that the alkali promoted Ni/YSZ sample improved catalytic performance, attributed to the reduction of coking.

Acknowledgements

I would like to express my gratitude to my supervisors Professor Thomas Willum Hansen (DTU), Professor Reine Wallenberg (LU) and examiner Professor Jan-Olle Malm (LU) for their unwavering support and guidance throughout my thesis. I am very grateful for the opportunity to collaborate with the Technical University of Denmark under Professor Thomas Willum Hansen's supervision. A special thank you to Professor Søren Kegnæs and his team, department of Chemistry (DTU), for letting me base my thesis on their research, and for their invaluable guidance. Finally, I would like to express my gratitude to Lund University, for the exceptional education and cherished memories during my time here, and to my friends and family for their support throughout this journey.

Table of contents

1 | Introduction

Increasing emissions of greenhouse gases (GHGs) causing global warming, has become an urgent worldwide concern. Carbon dioxide (CO_2) and methane (CH_4) have become predominant GHGs due to their high emissions. The primary contributor to CO_2 and CH_4 emissions today is the energy production, including fuels for energy and transportation, and raw materials for the chemical industry. To reduce GHGs emissions, developing methods of capturing, utilizing, and storing these gases is crucial. Dry reforming of methane (DRM) is a process that has gained a lot of attention as a carbon utilizing technology. DRM is the chemical process to produce syngas, a mixture of hydrogen (H_2) and carbon monoxide (CO), by utilising CH_4 and CO_2 (Eq. 1) [1, 2], see Fig. 1. DRM is primarily used for hydrogen production, and syngas ($CO+H_2$) is a vital intermediate in the industry for bulk chemicals syntheses, and hydrocarbon fuels production, such as diesel fuel and methanol [3, 4]. Furthermore, the DRM reaction can under optimal conditions produce syngas with an ideal molar ratio ($H_2/CO \approx 1$), making it favourable for the Fisher-Tropsch synthesis of liquid hydrocarbons utilised as fuels [7].

The DRM process is highly endothermic, requiring operating temperatures of 700-1000°C. To promote the reaction and achieve favourable conversion rates, nanoparticle catalysts dispersed onto supporting material are commonly used [2]. The usage of noble metal catalysts such as Pd, Ru and Rh have been studied due to their high thermal stability, and enhanced resistance to coking and sintering compared to other elements. However, due to high costs and resource limitations, they remain unsuitable for industrialization [5, 6]. Thus, transition metals such a Fe, Co, Zr and Ni have been studied for DRM. Particularly, Ni has emerged as a popular catalyst of choice owing to its cost-effectiveness, abundance, and exceptional catalytic activity. However, at high temperatures (>700°C), sintering (particle agglomeration), and coking (carbon formation on the catalyst surface) is inevitable. This ultimately results in the deactivation of the Ni catalysts [7].

Steam reforming of methane (SRM) and partial oxidation (POX) remain as of today the leading techniques for hydrogen and syngas production. In contrast to DRM, SRM utilises H_2O, instead of CO_2, to oxidise CH_4 (Eq. 2), and POX utilises O_2 (Eq. 3). Neither SRM nor POX involve utilising GHGs CO_2 as a reactant, however, similar to DRM, both processes encounter issues with coking and sintering, leading to catalyst deactivation [7, 8]. Finding solutions to prevent the catalyst deactivation in DRM can therefore have an immense positive impact on the reduction of GHGs compared to SRM and POX.

There are different methods currently being investigated to prevent coke formation and sintering on Ni catalysts, including using alkali elements, alkaline earth elements, or transition metals as promoters, encapsulating Ni in mesoporous materials, dispersing Ni in metal oxides chemically or physically, or encapsulating Ni catalysts in an inorganic shell. Additionally, strong catalyst-support interaction, basic/acidic properties of the support, and thermally stable nanoparticle catalysts with sizes below 10 nm for higher surface area, have shown better resilience towards sintering and coke formation and thereby improving catalytic activity [3, 6, 7].

$CH_4\,(g) + CO_2\,(g) \rightarrow 2CO\,(g) + 2H_2\,(g)$	$\Delta H°_{298K} = +247$ kJ/mol	(Eq. 1)
$CH_4\,(g) + H_2O\,(g) \rightarrow CO\,(g) + 3H_2\,(g)$	$\Delta H°_{298K} = +206$ kJ/mol	(Eq. 2)
$CH_4\,(g) + ½O_2$ -> $CO\,(g) + 2H_2\,(g)$	$\Delta H°_{298K} = -36$ kJ/mol	(Eq. 3)

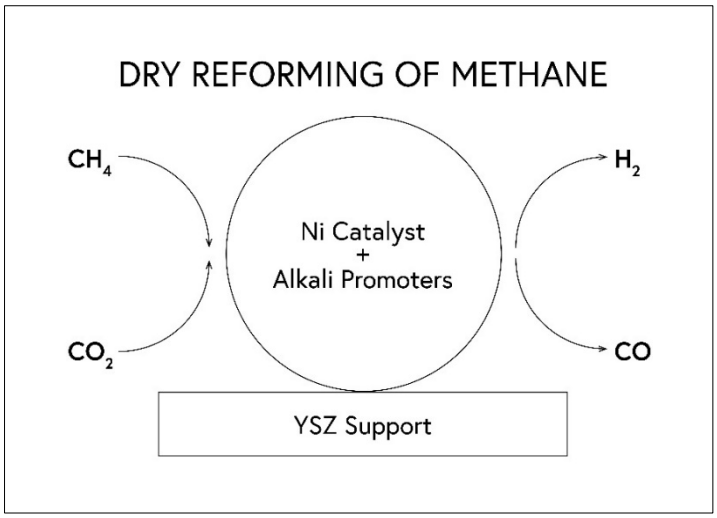

Fig. 1. Schematic of the DRM reaction: CH_4 and CO_2 react to form CO and H_2 with the help of catalysts. In this thesis Ni catalysts on YSZ support, with and without added alkali promoters, were examined.

2 | Aim

In this thesis, the impact of added alkali promoters to Ni catalysts on yttria-stabilised zirconia (YSZ) support is examined and aims to determine whether these alkali promotions enhance overall catalytic activity, by reducing carbon growth and sintering of the catalytic Ni nanoparticles. Four samples of 5 wt% Ni catalysts on YSZ supports: pre and post DRM reaction, promoted and unpromoted, are examined using TEM imaging to analyse coking and STEM-XEDS mapping to analyse sintering.

3 | Background

3.1 | Dry Reforming of Methane

DRM is a chemical process involving the reaction of CO_2 and CH_4 to produce syngas, a mixture of CO and H_2 (Eq. 1). This highly endothermic reaction requires high temperatures of 700-1000°C, atmospheric pressure, and catalysts to promote the reaction and to achieve high conversion rates [7]. The elevated temperature, while necessary for the DRM reaction, also promotes unwanted particle agglomeration (sintering). In addition to the desired DRM reaction, several side reactions occur, resulting in the formation of undesired carbon deposition (coking) on the Ni catalyst surface, (Eq. 4-7). Coking and sintering ultimately lead to the deactivation of the Ni catalysts, resulting in lower hydrogen production yield. Furthermore, maintaining a syngas H_2/CO molar ratio close to 1 (H_2/CO ≈ 1) is essential for further utilization as feedstock for the Fisher-Tropsch synthesis, however, also serves as a key indicator for preventing unwanted coking. A ratio exceeding 1 signifies an excess of H_2 production, indicating CO is lost through carbon formation on the surface (coking) by the Boudouard reaction (Eq. 5). Alternatively, a ratio below 1 indicates increased CO production, where H_2 is lost in a reducing reaction with CO_2 or CO, resulting as well in undesired coking (Eq. 6-7) [7, 9]. Moreover, the reverse water-gas shift (RWGS) reaction (Eq. 8) pushes the H_2/CO ratio below 1, and with the increased resulting CO, further contributes to coke formation (Eq. 5-7). The RWGS reaction is however less significant at higher operating temperatures as the DRM reaction is more endothermic and thus more favoured [8].

CH_4 (g) → C (s) + $2H_2$ (g)	$\Delta H°_{298K}$ = + 74.9 kJ/mol	(Eq. 4)
2CO (g) → CO_2 (g) + C (s)	$\Delta H°_{298K}$ = - 172.4 kJ/mol	(Eq. 5)
CO_2 (g) + $2H_2$ (g) → C (s) + $2H_2O$ (g)	$\Delta H°_{298K}$ = - 90 kJ/mol	(Eq. 6)
CO (g) + H_2 (g) → C (s) + H_2O (g)	$\Delta H°_{298K}$ = - 131.3 kJ/mol	(Eq. 7)
CO_2 (g) + H_2 (g) → CO (g) + H_2O (g)	$\Delta H°_{298K}$ = + 41 kJ/mol	(Eq. 8)

The addition of catalysts to the DRM process serve to decrease the activation energy of the reaction, enhance reaction rates, and improve selectivity for the main reaction (Eq. 1) over side reactions (Eq. 4-8). An ideal catalyst would maintain a good activity over time and resist sintering and coking; however, such catalysts do not exist. While noble metals are more resistant to coking and sintering than other catalysts, they are costly and scarce. Alternatively, highly dispersed Ni nanoparticles on metal-oxide supports, with the addition of alkali promoters, have shown promising results. These catalysts exhibit high initial activity and maintain good thermal stability under challenging operating conditions (>700°C), while remaining cost-efficient and abundant [6, 27].

3.2 | Catalyst Deactivation – Coking and Sintering

Catalyst deactivation occurs over time due to various factors, including sulphur poisoning; sulphur impurities blocking the active sites of the Ni catalyst, thermal degradation, coking and sintering [4]. This thesis focuses on catalyst deactivation due to coking and sintering.

3.2.1 | Coking

Coking occurs when carbon (C) produced from the side reactions covers the Ni catalysts, blocking the active sites. This coating prevents reactants from accessing the active sites, ultimately leading to catalyst deactivation [5, 10]. As previously mentioned, operating within the temperature range of 700-1000°C has been shown to be optimal for achieving higher hydrogen production yield, however also for reducing coking during DRM. At these elevated temperatures, the decomposition of methane (Eq. 4), is the side reaction most prone to occur based on its thermodynamic nature, in contrast to the less favoured side reactions (Eq. 5-8). The decomposition of methane occurs over the Ni surface, where the produced C atoms may either react with surrounding H_2O, O_2, CO_2, or H_2, react with the Ni particles forming Ni_3C, or initiate the formation of carbon layers on the Ni surface. Both crystalline and amorphous carbon can grow on the Ni particles, a topic that will be discussed further in Section 3.4. However, the formation of carbon layers is only initiated when C atoms cover more than approximately 80 Ni atoms, owing to thermodynamic stability [7]. Hence, the aggregation of Ni particles (sintering), which increases the Ni particle sizes and the number of Ni atoms within the particle, will inevitably lead to the initiation of coking. It is therefore crucial to keep the Ni particle sizes small. Nevertheless, some extent of sintering will inevitably occur when operating at temperatures above 700°C [7, 10].

3.2.2 | Sintering

Sintering is an irreversible process where particles agglomerate together, often at higher temperatures, resulting in the formation of larger particles. This leads to a reduction in surface area, and when these particles serve as catalysts, it results in a decrease in surface area of active sites leading to decreased catalytic activity. There are two types of mechanisms for sintering: particle migration and coalescence (PMC), and Ostwald ripening (OR). PMC involves adjacent particles merging into a larger particle, driven by diffusion and minimization of

surface energy. Elevated temperatures increase the thermal energy of the particles, overcoming diffusion energy barriers and moving more freely across the surface of the support. As a result of increased movement, particles experience more frequent collisions and merging. This merging process is energetically favoured as it minimises the total surface area and thus the total surface energy when a larger particle is formed from two smaller ones. OR is the process of larger particles growing at the expense of smaller particles, driven by the difference in surface energy. Smaller particles have higher surface energy compared to larger particles and it is this difference that drives single or clusters of atoms from smaller particles to move towards adjacent larger particles, promoting their merging and subsequent growth. Both PMC and OR occur simultaneously, where one can be more prominent depending on reaction conditions. In the early stages of the reaction when the particles are small, PMC may be favoured as diffusion has a more pronounced effect**,** leading to more frequent collisions. As the nanoparticles grow, the mobility of these particles decreases, and the diffusion is less pronounced [11, 12].

3.3 | The DRM Reaction and the Effect of Supports and Promoters

There are two main steps of the DRM reaction (Eq. 1): the decomposition of methane (Eq. 4) followed by the decomposition of carbon dioxide (Eq. 9). Once CH_4 adsorbs onto the Ni surface the decomposition can occur. CH_4 is more energetically favoured to be adsorbed at Ni step sites compared to terrace sites, which can also account for the higher catalytic activity observed in smaller Ni particles, as smaller Ni particles have more step atoms per unit mass than larger Ni particles. The CH_4 is then split into carbon species (CH_3, CH_2, CH, C) that remain adsorbed on the Ni surface (Eq. 4). The carbon species must undergo oxidation and form CO, in order to desorb from the Ni surface and make space for new CH_4 molecules to adsorb to the active site of the catalyst. This is done by the decomposition of CO_2 (Eq. 9), where the resulting O_2 oxidises the carbon species into the resulting product CO, completing the DRM reaction (Eq. 1). The two reactions: decomposition of methane and decomposition of carbon dioxide, occur simultaneously, however depending on reaction conditions, choice of support and promoters, one of the reactions may be favoured.

$CH_4\ (g) + CO_2\ (g) \rightarrow 2CO\ (g) + 2H_2\ (g)$	$\Delta H°_{298K} = +\ 247$ kJ/mol	(Eq. 1)
$CH_4\ (g) \rightarrow C\ (s) + 2H_2\ (g)$	$\Delta H°_{298K} = +\ 74.9$ kJ/mol	(Eq. 4)
$CO_2\ (g) \rightarrow CO\ (g) + ½\ O_2\ (g)$	$\Delta H°_{298K} = 532.2$ kJ/mol	(Eq. 9)

The DRM reaction is affected by the choice of support. Ni catalysts dispersed on metal-oxide supports such as SiO_2, MgO, ZrO_2, display high activity and enhanced thermal stability under challenging operating conditions, such as high temperatures. Acidic metal-oxide supports, such as SiO_2, have been shown to favour methane absorption on their acidic surface. This promotes methane decomposition rather than carbon dioxide decomposition, resulting in more carbon species remaining on the Ni surface, leading to increased coking, see Fig. 2. Note that decomposition of methane is the first step of the DRM reaction (Eq. 1) but also the side reaction (Eq. 4) contribution to coking if the reaction is favoured over the decomposition of carbon dioxide (Eq. 9). In contrast, basic metal-oxide supports such as MgO have shown the opposite, promoting carbon dioxide decomposition and could lead to suppression of carbon formation. Other supports, such as ZrO_2, have shown to supply oxygen from their lattice that in turn help oxidise the carbon species on the Ni catalyst surface, contributing to the suppression of carbon growth. Furthermore, ZrO_2 is commonly used as a support due to its excellent thermal stability and mixture of acid-base surface properties [7, 8, 13].

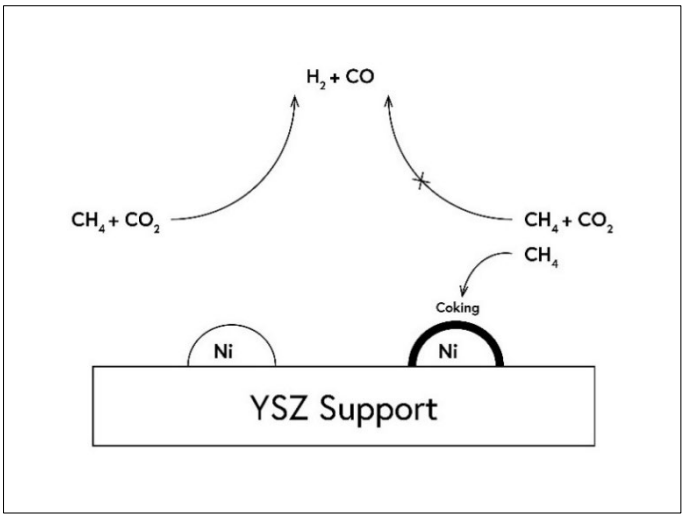

Fig. 2. Schematic of the DRM reaction with Ni catalysts on YSZ support: on the left side, the DRM reaction occurs with the aid of the Ni catalyst, while on the right side, the reaction is inhibited due to coking formed from methane decomposition, blocking the active sites of the Ni catalyst.

YSZ, zirconia (ZrO_2) doped with yttria (Y_2O_3), has shown excellent support properties. By doping ZrO_2 with Y_2O_3, oxygen lattice vacancies are created as some of the Zr^{4+} ions are replaced by Y^{3+}, see Fig. 3**.** These oxygen vacancies serve as active sites for the dissociation of O_2 molecules into O^- ions, that can then transfer through the YSZ lattice to the YSZ-catalyst interface [25]. From there the O^- ions can diffuse to the Ni catalytic active sites and participate in the DRM reaction, and at the same time take care of carbon species that would lead to coking. Furthermore, the presence of these oxygen vacancies allows for faster oxygen diffusion through the YSZ crystal, enhancing reaction rates. YSZ exhibits basic properties due to the presence of these oxygen vacancies, allowing it to accept oxygen in the form of ions. Yttria further help stabilise zirconia in its cubic fluorite crystal phase, ensuring durability under high temperatures, and enhanced oxygen conductivity [20, 25].

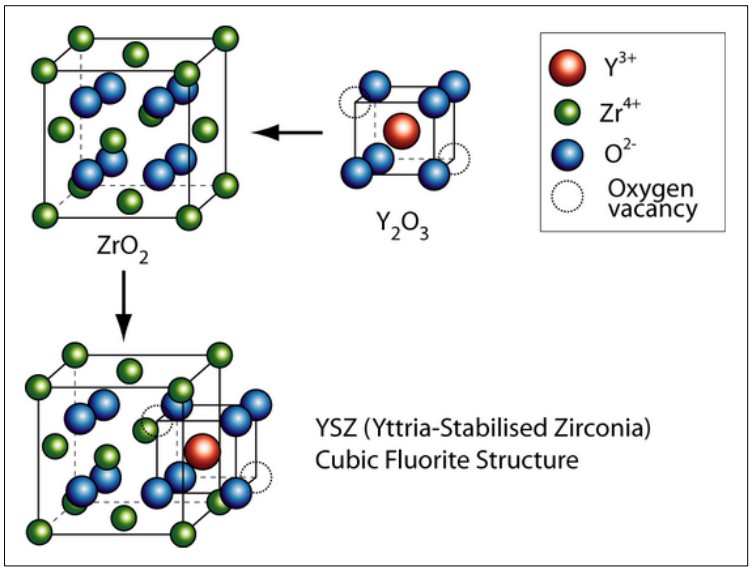

Fig. 3. The cubic fluorite structure of YSZ; zirconia doped with yttria, highlighting the created oxygen vacancies. Image taken from reference [29].

In addition to using a suitable support, alkali and alkaline earth promoters have been shown to reduce coking. Adding basic promoters such as K, Na, Ca, and Mg to the Ni catalyst can enhance the CO_2 adsorption, facilitating its dissociation. These basic promoters also deactivate acidic sites on the catalyst and support, leading to reduced coking [10, 27]. However, it is important to note that the support and the promoters increasing the basicity and reducing coking, may in fact also contribute to coking. Promoting CO_2 dissociation leads to increased production of CO and O_2 (Eq. 9), which further promotes the Boudouard reaction (Eq. 5), producing more carbon atoms on the catalyst surface. Furthermore, an excessive quantity of atomic oxygen may oxidise Ni atoms into nickel oxide (NiO), also leading to catalyst deactivation. Thus, achieving the correct balance between acidity and basicity for the Ni catalyst environment can be crucial when selecting supports and promoters, in order to reduce coking [10].

Promoters could furthermore help strengthen the catalyst-support interaction. A study by *Gao et al. (2020)* showed that the addition of Ca promoters strengthened the interaction between Ni catalysts and Al_2O_3 support. A strong catalyst-support interaction can help reduce sintering by anchoring the catalyst particle onto the surface of the support. This limits particle diffusion across the sample, preventing particle agglomeration through coalescence [28].

Additionally, in a study by *Budhi et al. (2023)*, 1 wt% of Na, K, Ca, and Mg promoters were individually applied to four samples of 10 wt% Ni/$CeZrO_2$ (10 wt% Ni catalyst on support $CeZrO_2$). The samples were employed in a DRM reaction at 700°C and atmospheric pressure and compared to the unpromoted Ni/$CeZrO_2$, and to commercial SRM, over the duration of 240 minutes. The Mg-Ni/$CeZrO_2$ exhibited the highest catalytic activity with a conversion of 78% CH_4, 64% CO_2, a yield of 56% H_2 and 41% CO, and a H_2/CO ratio of 1.52. Compared to the unpromoted Ni/$CeZrO_2$, this was 5% and 10% higher CH_4 and CO_2 respectively, and 5% higher H_2 yield, and furthermore had 2.5 times higher CH_4 and CO_2 conversion than commercial SRM. Similarly, the Ca-Ni/$CeZrO_2$ displayed increased catalytic activity, surpassing the unpromoted Ni/$CeZrO_2$ but falling below the Mg-Ni/$CeZrO_2$. Furthermore, the Na-Ni/$CeZrO_2$ exhibited the lowest level of coking, with only 10% carbon growth, followed by 20% for K, 25% for Ca, 30% Mg and 35% for commercial SRM [13].

These findings highlight the multitude of factors impacting catalytic activity and stability. While the focus is on different alkali and alkaline earth promoters (Mg, K, Ca, Na) on 10 wt% Ni/$CeZrO_2$, the inclusion of various supports, other types of promoters, diverse reaction conditions, and varying weight percent (wt%) of Ni particles and promoters will introduce further variability in the outcome. Research in the field of DRM is ongoing, exploring various reaction conditions to achieve the optimal setup for the best catalytic activity and production yield.

3.4 | Coking – Formation of Carbon Structures

Various carbon structures can form on the Ni catalysts during the DRM process, including amorphous, turbostratic, and graphene carbon, see Fig. 4. Furthermore, carbon atoms can interact with Ni atoms forming nickel carbide (Ni_3C)**.** Amorphous carbon is characterised by its disordered structure, lacking a well-defined crystalline arrangement. Turbostratic carbon exhibits a random and disordered arrangement of graphene layers, lacking long-range order, resembling both amorphous and graphene carbon. Graphene consists of individual layers of carbon atoms arranged in a two-dimensional hexagonal lattice, and can form tubular shapes,

called carbon nanotubes (CNTs). These CNTs can be single walled or multi walled, consisting of single or multiple layers of graphene sheets. The formation of these carbon structures occurs within specific temperature ranges, see Table 1. These various structures can be distinguished through imaging methods, such as TEM, and detected by temperature programmed oxidation (TPO) [8, 10, 14].

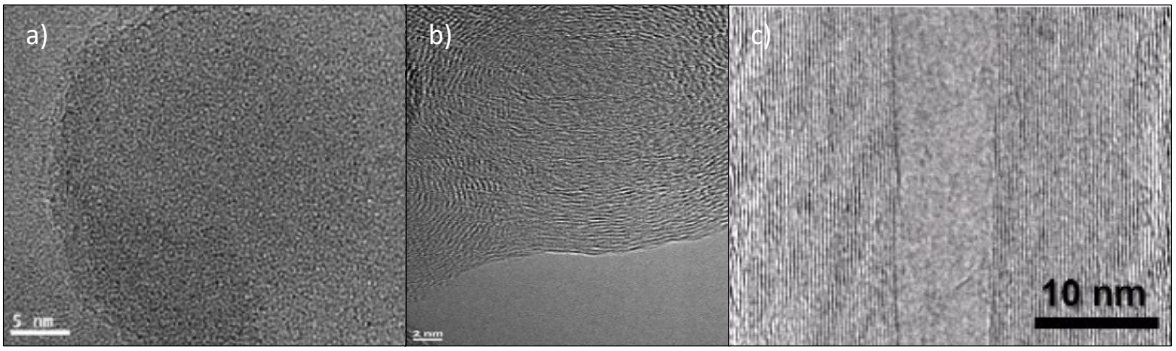

Fig. 4. TEM images of various carbon structures. Images taken from reference [22] showing amorphous carbon (a), [21] showing turbostratic carbon (b), and [23] showing graphene carbon forming a CNT (c).

Table 1. Formation temperature of various carbon structures growing on Ni catalysts [10].

Carbon structure	**Temperature of formation (°C)**
Amorphous	250-500
Graphene/CNTs	300-1000
Nickel carbide	150-250

3.4.1 | Temperature Programmed Oxidation

TPO is a technique used for analysing surface properties of materials and can be used to detect coking on the surface of the catalyst and support. TPO uses oxygen to oxidise the carbon structures grown on the surface. The principle behind TPO is as follows: A sample with spent catalysts (post DRM reaction) is inserted into the TPO reactor. The sample is flushed with an inert gas, such as nitrogen, to eliminate any residual gases or contaminants. An oxidising gas, such as air or oxygen, is supplied to the reactor and oxidises the carbon structures grown on the sample into carbon species, such as CO and CO_2. Simultaneously the temperature of the sample is increased at a controlled slow rate. The resulting CO_2 is then measured by a gas chromatograph, registering the concentration of CO_2 as a function of temperature. The various forms of carbon structures oxidise at different temperatures, which appear as peaks on the TPO graph. The temperature where the peaks are present are indicators to which carbon structure corresponds to which peak, revealing the amount present of each carbon structure. Combining this data with TEM imaging can provide a more comprehensive profile of the existing carbon structures [10, 14, 15].

3.4.2 | Mechanism of Carbon Growth on Ni Particles

Coking can occur on both the support and the Ni particles, however the problem arises when the Ni catalyst particles become coated with carbon growth, blocking the active sites. *Helveg et al. (2004)* studied the formation of CNTs on 5-20 nm sized Ni particles supported on $MgAl_2O_4$ and found the following: The formation of CNTs begins with the adsorption of an adequate number of carbon atoms onto the Ni surface, initiating the formation of the first graphene layer [16]. The first layer then helps facilitate the growth of a second layer at the Ni-

graphene sheet interface. This process is driven by the adsorbed C atoms (from the first graphene sheet) inducing the formation of step edges on the Ni surface. This occurs because the binding energy between the adsorbed C atoms and the Ni atoms is greater than the energy cost for step edge formation. Consequently, energy is gained from step edge formation, releasing Ni atoms previously bound at the Ni-graphene interface. The free Ni atoms diffuse away from the interface towards the free-of-graphene Ni surface, while free C atoms diffuse towards the interface, contributing to the growth of a new graphene layer in between a pair of step edges on the Ni surface, see Figs. 5 and 6(a-f). This process is repeated and results in the generation of multiple graphene sheets that grow with their crystal planes parallel to the Ni surface, taking on the shape of a tube with the Ni particle inside. Furthermore, the ongoing removal of Ni particles to the free-of-graphene Ni surface and the replacement of carbon atoms forming graphene sheets, cause the Ni particle to elongate. This elongation continues until the Ni particle length/width ratio reaches approximately 4. At this stage, the surface energy of the Ni particle has increased due to the elongation and is no longer able to compensate for the energy gained from the binding of the graphene layer to the Ni surface. The Ni particle bounces back into its spherical shape, see Fig. 6(g-h), moving away from its initial position and leaving behind a hollow space with nearly parallel graphene sheets, forming a multi-walled CNT. The CNT continues to grow in length as the elongation/ contraction process is repeated, ceasing growth only when the graphene layers fully encapsulate the entire Ni particle. Furthermore, if the crystal planes of the graphene sheets grow inclined with respect to the CNT growth axis, it results in the formation of carbon whisker, see Fig. 7. *Helveg et al. (2004)* found that this is typically associated with larger Ni particles, where the Ni particle undergoes non-unform elongation, often assuming a pear shape, thus affecting the growth direction of the graphene sheets [16].

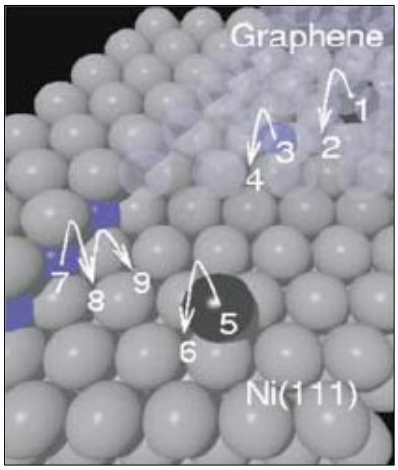

Fig. 5. Image taken from *Helveg et al. (2004)* [16], showing the diffusion of free carbon atoms (colour purple) in the Ni-graphene sheet interface (colour light grey: bulk Ni atoms, colour transparent: carbon atoms as a graphene sheet). It is at this Ni-graphene sheet interface where free carbon atoms diffuse towards, and free Ni atoms diffuse away from, forming step edges (not visible) in the Ni bulk, giving space for the free C atoms to form a new graphene sheet. Number 1-9 serve to illustrate energy barriers resulting from different diffusion paths for the various atoms, a topic that is beyond the scope of this thesis.

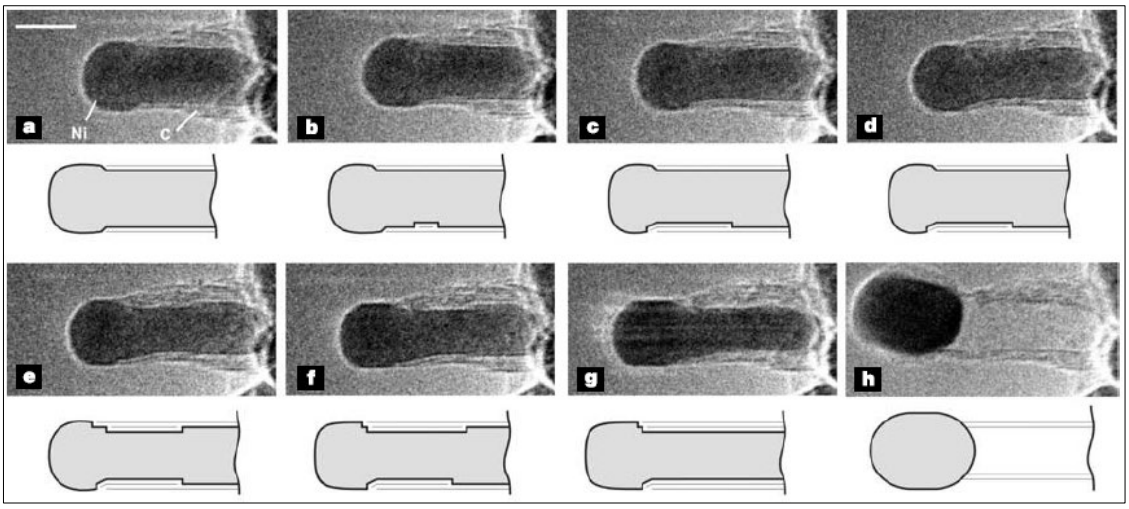

Fig. 6. Image taken from *Helveg et al. (2004)* [16], showing the growth process of graphene sheets on the Ni particle. Step edges are introduced at the Ni-graphene sheet interface as a result of Ni atoms diffusing away from the Ni-graphene sheet interface and towards the free Ni surface, making space for free C atoms to diffuse into the Ni-graphene interface to form a new graphene layer (a-f). This process is then repeated for the formation of additional graphene layers, causing the elongation and relaxation of Ni particle, leaving behind a formed multi walled CNT (g-h).

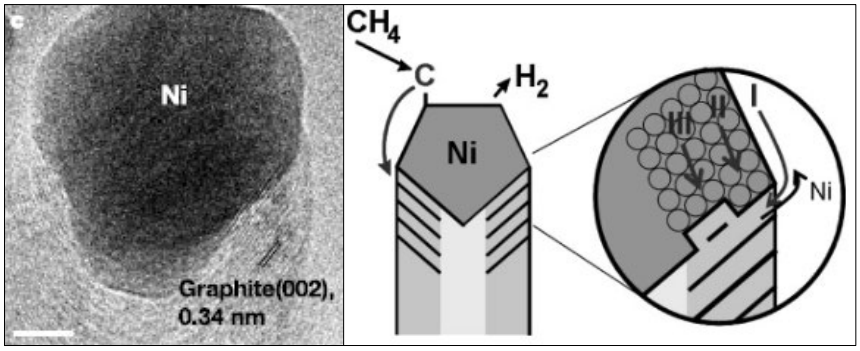

Fig. 7. Images taken from *Helveg et al. (2004)* [16] showing carbon whiskers, where graphene sheets grow inclined in respect to the CNT growth axis.

3.5 | Transmission Electron Microscopy

The TEM was invented by Knoll and Ruska in 1932 and is an exceptional instrument capable of analysing and visualising samples with sub-Ångström resolution. It is a great tool for studying catalysts, providing detailed information of the size, shape, morphology, crystallography, and chemical composition of the sample.

The fundamental principle of a TEM is as follows: Electrons are emitted from the electron source, which can be either a thermionic gun or a field emission gun (FEG). The thermionic electron source is in the form of a V-shaped filament, typically composed of materials such as LaB_6 or W, while the FEG consists of a needle-shaped W tip. In thermionic emission, the source is heated sufficiently for the electrons to overcome the work function of the material, causing electron emission. For a FEG, a high voltage is placed between the cathode source and an anode, and electrons are emitted as a result of the created electric field. For both thermionic and FEG sources, the emitted electrons are accelerated by a second anode [17, 18]. Fig. 8 shows a schematic of a TEM.

Below the electron source, electromagnetic condenser lenses and apertures are positioned to create a coherent and focused electron beam directed onto the sample. The electron beam can be focused into a parallel or convergent beam, allowing the microscope to operate in the modes: transmission electron microscope (TEM) or scanning transmission electron microscope (STEM). As the beam interacts with the atoms of the sample, the electrons undergo elastic or inelastic scattering. Elastic scattering is the process where electrons interact with atoms without transferring energy. Respectively, inelastic scattering is the process where electrons lose energy to atoms upon interaction. Elastic scattered electrons are used for creating an image and a diffraction pattern, providing structural and crystallographic information of the sample, whereas inelastic scattered electrons are used for energy-dispersive X-ray spectroscopy (XEDS) and electron-energy loss spectrometry (EELS), providing information of the chemical composition of the sample.

The scattered electrons exiting the sample are focused by the objective lens, forming a diffraction pattern in the back focal plane (BFP), and with the help of electromagnetic lenses a magnified image of the sample is formed in the image plane, see Fig. 8(b). A detector is placed in the image plane to record the image, this can be a fluorescent screen, or as in most modern TEM, a charge-coupled device (CCD) camera. The CCD camera converts the incoming electron signals into digital signals that are displayed on a computer screen.

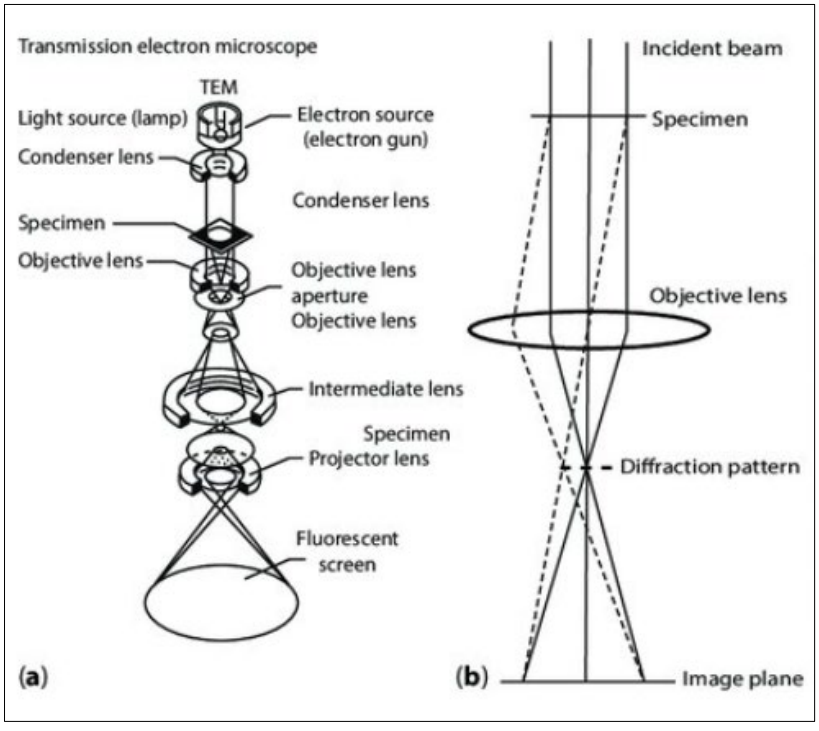

Fig. 8. Schematic image of a TEM, highlighting the key components. Image taken from reference [25].

There are two imaging options for TEM**,** dark field (DF) and bright field (BF) imaging. In BF TEM imaging, an aperture in the BFP allows only the unscattered and low angle scattered elastic electrons to pass. These correspond to the central bright spot (direct beam) in the diffraction pattern. Respectively, in DF TEM imaging, an aperture is placed over specific diffraction spots, allowing only scattered elastic electrons to pass while blocking the central unscattered beam. For BF imaging this gives rise to a contrasted image where unscattered elastic electrons are collected by the detector and appear bright in the image, and the scattered electrons do not

contribute. The opposite holds for DF imaging. Fig. 9 shows a TEM image and a diffraction pattern. The diffraction pattern holds crystallographic information of the whole area analysed. Furthermore, it is possible to generate an image similar to a diffraction pattern, by applying a Fast Fourier Transform (FFT) to the TEM image. FFT is a mathematical tool that translates the spatial information of the image into its frequency domain, revealing the periodicity of the area analysed, including its crystallinity and structural characteristics, similar to a diffraction pattern. Performing FFT allows for a more rapid processing alternative for TEM imaging.

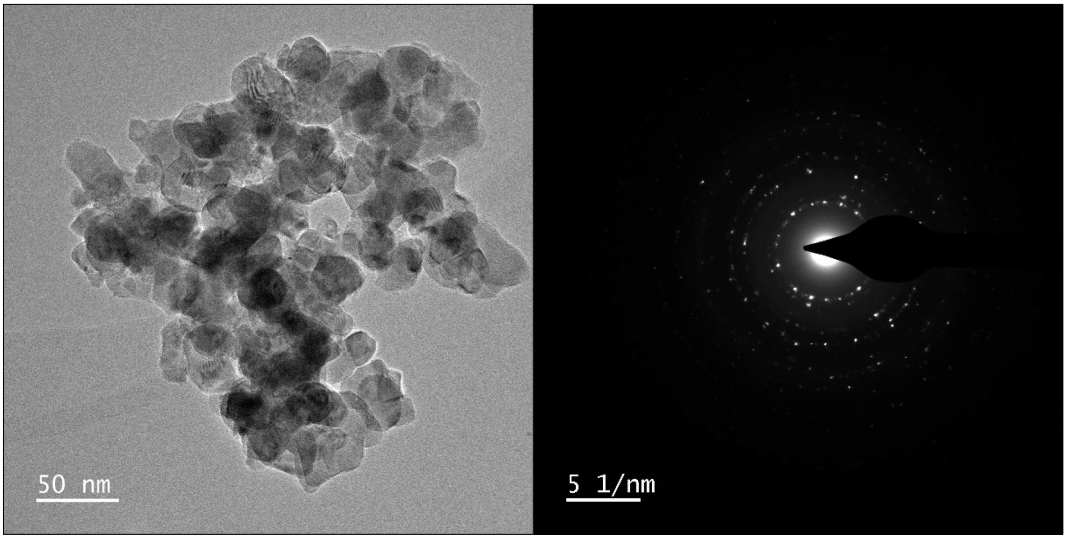

Fig. 9. TEM image of Ni particles on crystalline YSZ support, and the corresponding diffraction pattern.

The contrast created in the images is a consequence of three processes: mass-thickness, diffraction, and phase contrast. Mass-thickness contrast relies on electrons scattering more strongly to heavier atoms and thicker areas of the specimen. In the case of BF imaging, heavier elements and thicker areas of the specimen will appear darker, in contrast to lighter elements and thin areas. The background of the sample will always appear bright as electrons passing through it encounter no material giving scattering from. Diffraction contrast arises when electron waves diffracted from crystal lattice planes interact constructively or destructively, resulting in a diffraction pattern in the BFP. This pattern is then translated into image contrast. The crystals from which the electron waves constructively interact with each other will appear bright, while the crystals with destructive interference will appear dark. The image contrast is influenced by factors such as crystal orientation, thickness, and defects within the sample. For phase contrast, the phase of the electron waves is changed as the wave is diffracted. These phase differences are results of varying thickness and electron density of the sample and are translated into contrast in the final image, where constructive wave interference appear bright and destructive wave interference appear dark in the BF image. BF imaging is predominately sensitive to mass-thickness contrast, however, diffraction and phase contrast are also present, whereas diffraction contrast dominates in DF imaging [18].

Ultimately, BF imaging is chosen to study the overall structure of the sample, providing information of the overall density and thickness variations, whereas for information regarding crystal structure, orientation and defects, DF imaging is more optimal.

3.6 | Scanning Transmission Electron Microscopy

STEM is powerful mode within electron microscopy, allowing imaging, diffraction information, and spectroscopy to be collected simultaneously, while still providing atomic spatial resolution.

Unlike in TEM mode, where the electromagnetic lens system focuses the electrons to a parallel beam, in STEM mode the electrons are focused into a nanosized probe that is scanned over the area of interest, point by point. The electrons interact with the sample, and like in TEM mode, the scattered electrons exiting the sample are focused into the BFP by the objective lens, creating a diffraction pattern. There are three important detectors used for STEM imaging: the BF detector, the annular dark field (ADF) detector and the high-angle annular dark field (HAADF) detector. These detectors are placed in the BFP, where they collect the transmitted elastically scattered or unscattered electrons. As the electron beam is scanned point by point, the BF image and diffraction information image are constructed digitally from all the scanned points.

For BF imaging, the BF detector collects the unscattered and low angle scattered elastic electrons, corresponding the central spot in the diffraction pattern, respectively, for ADF imaging, the ADF detector collects all the scattered elastic electrons, corresponding to the surrounding diffraction spots within a certain angular angle, unlike DF TEM collecting only scattered electrons from one diffraction spot, see Fig. 10. Furthermore, a HAADF detector is placed outside the diffraction pattern collecting elastic electrons that have scattered at a very high angle (Rutherford scattering).

HAADF imaging is powerful tool that largely eliminates diffraction and phase contrast, showing primarily mass-thickness contrast. Unlike in BF and ADF modes, where the electrons are coherent, those collected in HAADF mode are incoherent. For diffraction and phase contrast to be visible, the electrons must be coherent, meaning the scattered electrons have a fixed phase relationship with each other and with the unscattered electrons (incident beam). This coherence allows for the formation of constructive and destructive interference producing a well-defined diffraction pattern.

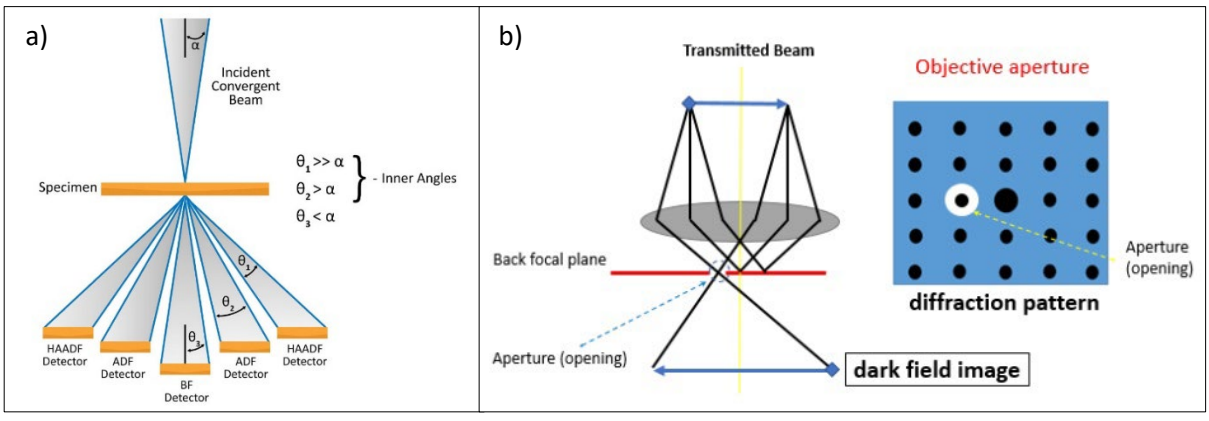

Fig. 10. Schematic images highlighting the differences of ADF STEM (a) and DF TEM (b): collecting scattered electrons from a wide angular range in the BFP using an annular detector (a). Selecting scattered electrons from a single diffraction spot in the BFP with the objective aperture, these electrons are used to construct the final image in the image plane, which is then recorded by the CCD camera (b). Images taken from reference [30, 31].

In HAADF mode, the lack of coherence means no well-defined diffraction pattern, thus eliminating diffraction and phase contrast. HAADF imaging therefore relies on mass-thickness contrast, where heavier atoms or thicker sample regions scatter more electrons, resulting in brighter contrast compared to lighter atoms or thinner regions. Consequently, the background in the image will appear dark, while the heavy elements and thicker areas will appear bright [18].

3.7 | Energy-Dispersive X-ray Spectroscopy

XEDS is a powerful electron microscopy technique, used for compositional analysis of the specimen. XEDS can be operated in both TEM and STEM mode and utilises characteristic X-rays generated through inelastic scattering.

As previously mentioned, inelastic scattering is the process where electrons lose energy when interacting with atoms and provides information of the chemical composition of the sample. As the beam hits the sample, electrons can interact inelastically with the nucleus or electron cloud of each atom, generating signals such as secondary electrons, Auger electron, cathodoluminescence and characteristic X-rays. Characteristic X-rays are created when an incoming electron interacts inelastically with a core shell electron. The core shell electron is ejected if enough energy is transferred to the core shell electron from the incoming electron, ionizing the atom, and leaving a hole in the core shell. The ionized atom can return to its ground state if the hole in the core shell is filled by an electron from an outer shell, and as this transition occurs an X-ray is emitted. As the hole can be filled from any outer shell, the emitted X-rays will have different energies, corresponding to the energy difference between the two electron shells. The energy differences between any two electron shells are unique for atoms of a specific element and are thus called characteristic X-rays. The characteristic X-rays are then collected by the XEDS detector, where X-ray counts are represented by spectra with peaks corresponding to specific X-rays energies, associated with a particular element. Analysing these peaks give a good indication of the elemental composition of the specimen. Furthermore, elemental maps can be constructed from the acquired X-ray spectra, giving the elemental spatial distribution of the sample. This method is particularly valuable for studying sintering processes, where distinguishing light elements (catalyst particles) on a heavier element (support) is challenging with TEM/STEM imaging. XEDS mapping allows for the visualization of the particle distribution, and the average particle size can be calculated by measuring the individual particle sizes [18].

4 | Experimental

4.1 | Sample Preparation

All samples were prepared and provided by Professor Søren Kegnæs and his team, department of Chemistry, DTU. The samples were received in powder form and were then prepared for TEM using a mortar and pestle, and then mounted on a carbon coated Au grid and inserted into the TEM.

4.2 | Catalyst Characterization

The TEMs and all equipment used was provided by the National Centre for Nano fabrication and characterization, Nanolab DTU.

4.2.1 | STEM-XEDS

Fresh and spent catalyst samples were characterised using STEM mode in the Titan E-cell 80-300ST TEM, equipped with a FEG and operated at an accelerating voltage of 300 kV. A Fischione HAADF detector was used for STEM mode imaging and a X-Max 80 mm^2 detector for XEDS mapping. The acquired XEDS data was analysed using the AZtec software from Oxford Instruments.

4.2.2 | TEM

Fresh and spent samples were characterised using two TEMs: (1) Tecnai T20 G2 S-TEM, equipped with a thermionic electron gun LaB_6 and operated at an accelerating voltage of 200 kV. A TVIPS XF416 CMOS 4K camera was used for acquiring images. (2) Titan E-cell 80-300ST TEM, equipped with a FEG and operated at an accelerating voltage of 300 kV. A Gatan OneView CMOS detector was used for acquiring images. All the images were analysed using the software GMS, Single Crystal and Crystal Maker.

4.2.3 | TPO and Catalyst Activity Measurements

TPO measurements of coking and measurements of catalyst activity were performed by Professor Søren Kegnæs and his team, and the obtained results were provided to give a broader comprehension from the findings of this thesis.

5 | Results and Discussion

This thesis investigates the effect of alkali promoted catalysts on coking and sintering during DRM reaction. Four samples of 5 wt% Ni catalysts on YSZ support were analysed pre and post DRM reaction, both with and without promoters. This thesis is based on the research of Professor Søren Kegnæs and his team, and due to confidentiality, the specific elements utilized as promoters and their corresponding weight percentages cannot be disclosed. TEM imaging was used to examine the various carbon structures grown on the surface (coking), and STEM-XEDS was used for mapping the agglomeration of the Ni catalyst particles (sintering). The Ni particles examined were found to be either pure Ni or had reacted with carbon or oxygen to form Ni_3C or NiO. Measurements of coking through TPO, and catalyst activity measurements were conducted by Professor Søren Kegnæs and his team, and the acquired data was provided for this thesis.

The samples will be denoted in the form of “post-alkali Ni/YSZ” for simplification, indicating the promoted sample post DRM reaction, refer to Table 2 for further details of all four samples.

Table 2. Labelling and conditions of the four samples examined for the DRM reaction.

Samples			
Pre Ni/YSZ	5 wt% Ni on YSZ	Pre reaction	Without promoters
Post Ni/YSZ	5 wt% Ni on YSZ	Post reaction	Without promoters
Pre-alkali Ni/YSZ	5 wt% Ni on YSZ	Pre reaction	With promoters
Post-alkali Ni/YSZ	5 wt% Ni on YSZ	Post reaction	With promoters

5.1 | TEM Imaging – Analysis of Coking

TEM imaging was used to get an overview of all four samples, and particularly examine potential differences in coking between the two samples post reaction, with and without promoters: post Ni/YSZ and post-alkali Ni/YSZ.

5.1.1 | Coking pre DRM Reaction – with and without Promoters

Representative images of samples pre Ni/YSZ and pre-alkali Ni/YSZ are shown in Figs. 11 and 12. By examining the particles where the lattice fringes are in focus, no CNTs or significant amount of amorphous carbon can be observed. This is expected as the samples have yet to undergo the DRM reaction, where coking is initiated. A few monolayers of amorphous carbon are visible in Fig. 11, however this occurrence is typical, as there is always some level of carbon growth due to sample contamination.

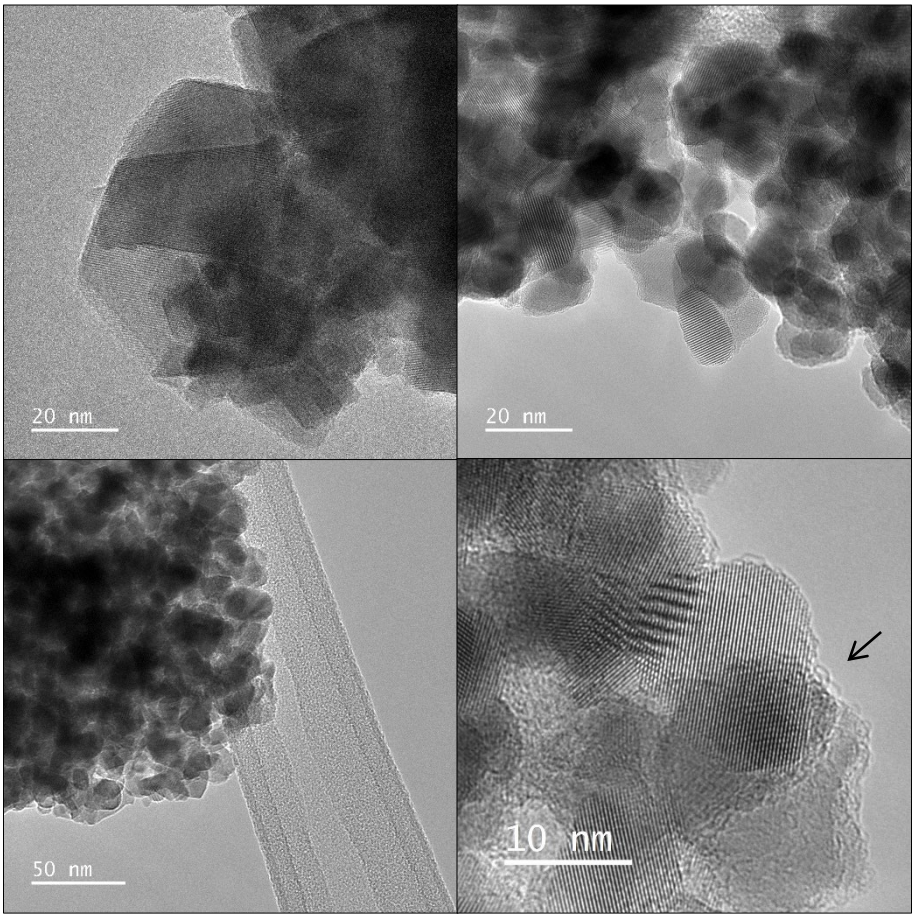

Fig. 11. TEM images from the Tecnai T20 G2 S-TEM of pre Ni/YSZ: pre reaction and without promoters. No CNTs or significant amount of amorphous carbon are visible. A few monolayers of amorphous carbon are present on the edge of a (YSZ) crystalline particles (see arrow).

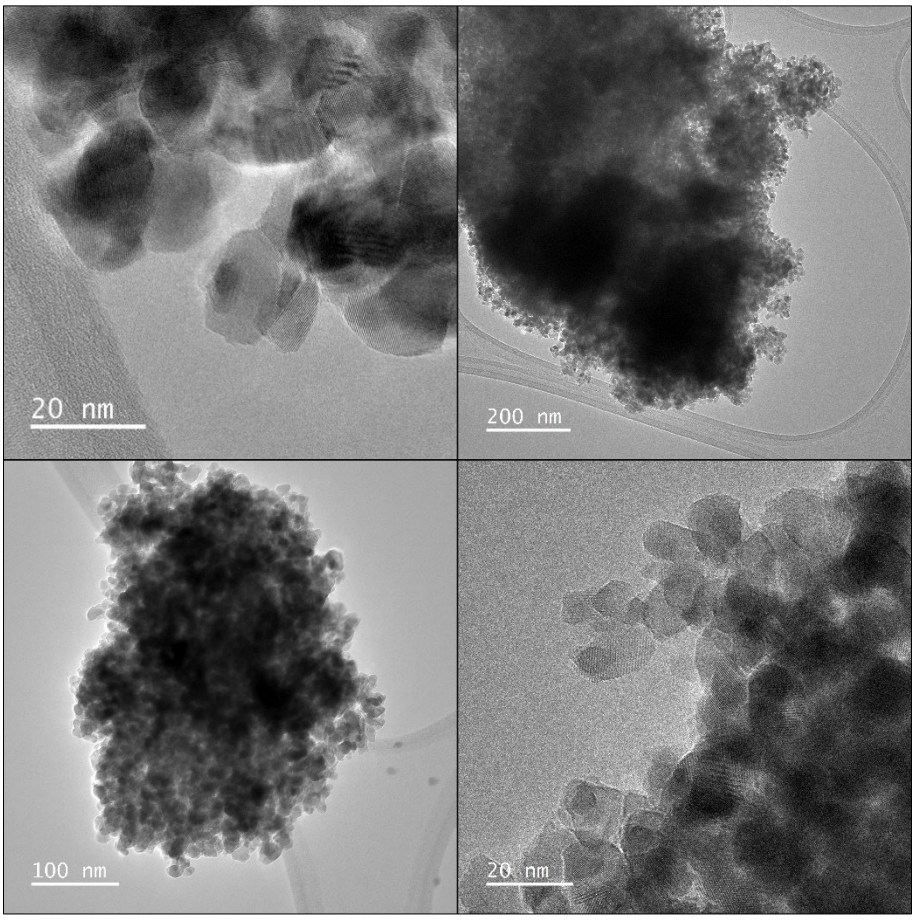

Fig. 12. TEM images from the Tecnai T20 G2 S-TEM of pre-alkali Ni/YSZ: pre reaction with promoters. No CNTs or significant amount of amorphous carbon are visible.

Both pre reaction samples show crystalline particles, and measurements of several lattice fringes in GMS reveal a crystal interplanar distance of approximately 2.9 Å, corresponding to the YSZ planes: YSZ{111} = 3.0 Å, as shown in Fig. 13. These TEM images were captured using the Tecnai T20 G2 S-TEM, with a spatial resolution of 2.0 Å in TEM mode, thus distinguishing lattice fringes under 2.0-2.5 Å poses a challenge. This makes it difficult to reveal the Ni particles on the YSZ particles, given that the interplanar distances for Ni, Ni_3C and NiO crystals are mostly <2.5 Å.

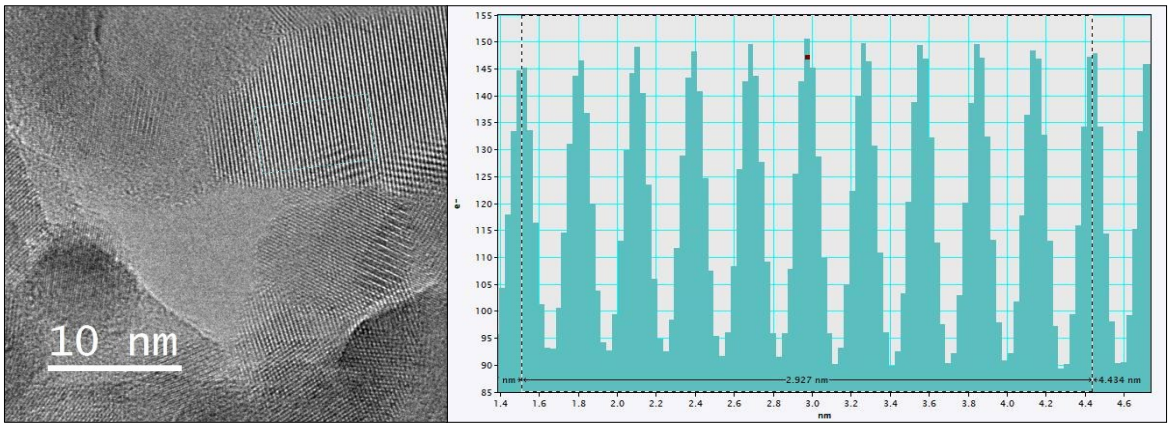

Fig. 13. Representative measurement of lattice fringes (right image) from the rectangular region in the TEM image (left image), using GMS software. The graph shows intensity as a function of distance (nm). The distance over 10 peaks is measured to 2.9 nm, corresponding to the average width per peak (lattice fringe), indicating the interplanar distance of YSZ{111}=3.0 Å.

5.1.2 | Coking post DRM Reaction - with and without Promoters

Coking was present in both post samples: post Ni/YSZ and post-alkali Ni/YSZ. TEM images were initially recorded by the Tecnai T20 G2 S-TEM, spatial resolution of 2.0 Å, however as previously mentioned, as the lattice fringes from the Ni particles were not visible, additional TEM images were also recorded by Titan E-cell 80-300ST TEM, spatial resolution 0.8 Å. Fig. 14 shows Ni particles encapsulated in CNTs, recorded by both TEMs. The lattice fringes of the CNTs encapsulating the Ni particles are clearly distinguishable in both cases. However, the lattice fringes of the Ni particles are only resolved in the images recorded by the by Titan E-cell 80-300ST TEM.

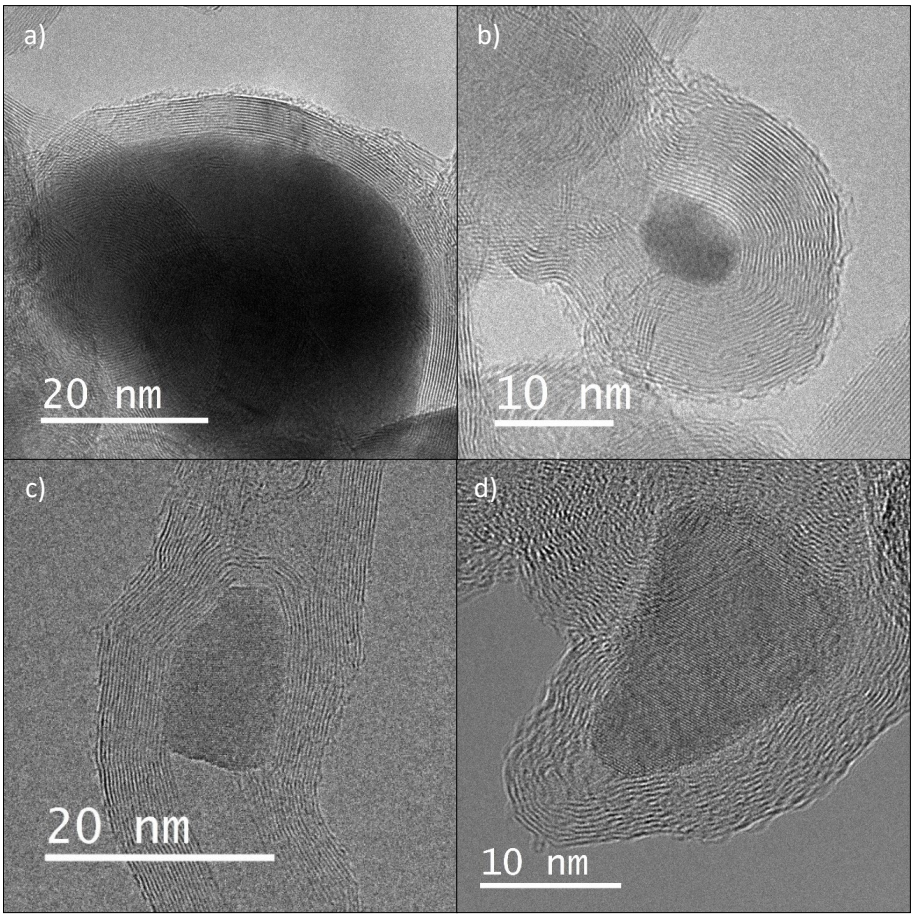

Fig. 14. TEM images recorded by the Tecnai T20 G2 S-TEM (a-b) and by Titan E-cell 80-300ST TEM (c-d). A Ni particle is encapsulated in a CNT and the Ni lattice fringes are not visible (a-b). A Ni particle is encapsulated in a CNT and the Ni lattice fringes are visible (c-d).

From low-magnification images, CNTs are prominently visible on nearly every analysed site in the post Ni/YSZ sample, see Fig. 15. In contrast, the post-alkali Ni/YSZ display significantly fewer sites with CNTs at this scale. Most sites appear either clear of CNTs or have very few, see Fig. 16(a-b), whereas few sites displayed more pronounced CNT growth, see Fig. 16(c).

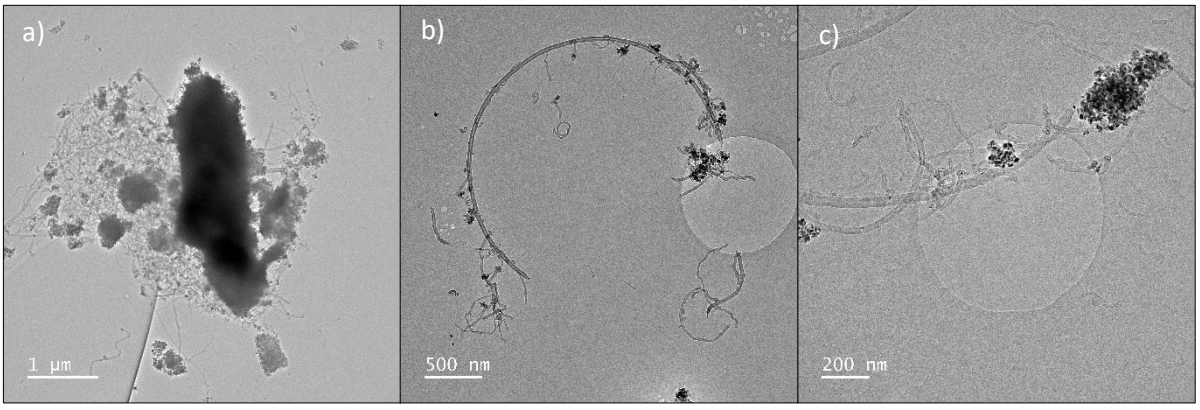

Fig. 15. Low-magnification TEM images of sample post Ni/YSZ. CNTs are visible on nearly all sites.

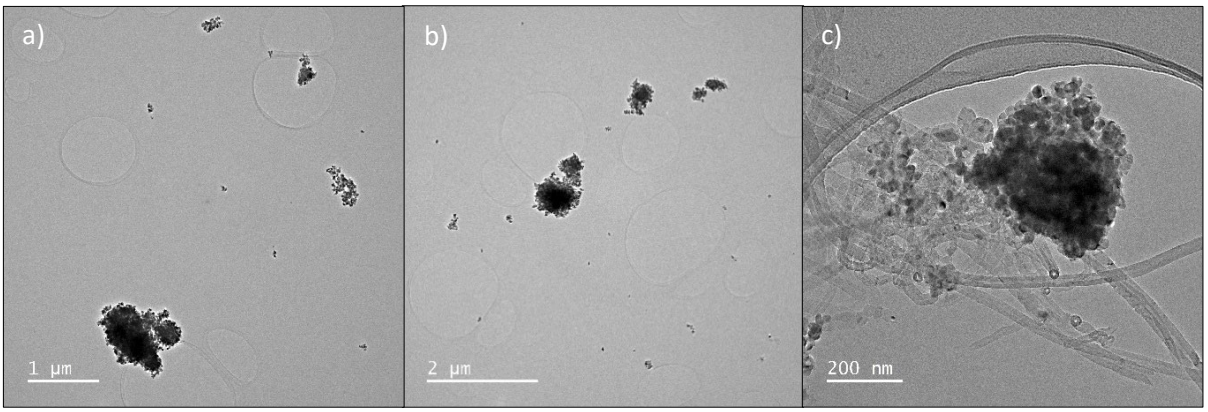

Fig. 16. Low-magnification TEM images of sample post-alkali Ni/YSZ. CNTs are visible on few sites.

5.1.3 | Carbon Nanotubes

The grown CNTs visible on samples post Ni/YSZ and post-alkali Ni/YSZ are multi-walled consisting of approximately 10-30 graphene sheets. Within the CNT structure, distinct segments that are terminated with caps are visible (a few layers of graphene sheets inside the CNT). It is possible that this marks the point where the CNTs initiate encapsulation around the Ni particles, however, the Ni particles elongate and bounce forward, further adding to the continued growth of the CNTs, as explained in Section 3.4.2, while leaving the caps behind, see Fig. 17. Even when a Ni particle is fully encapsulated in the middle of a CNT, continuous growth of the CNT can still be observed. This appears to be due to the presence of multiple Ni particles within the same CNT, together contributing to its ongoing growth.

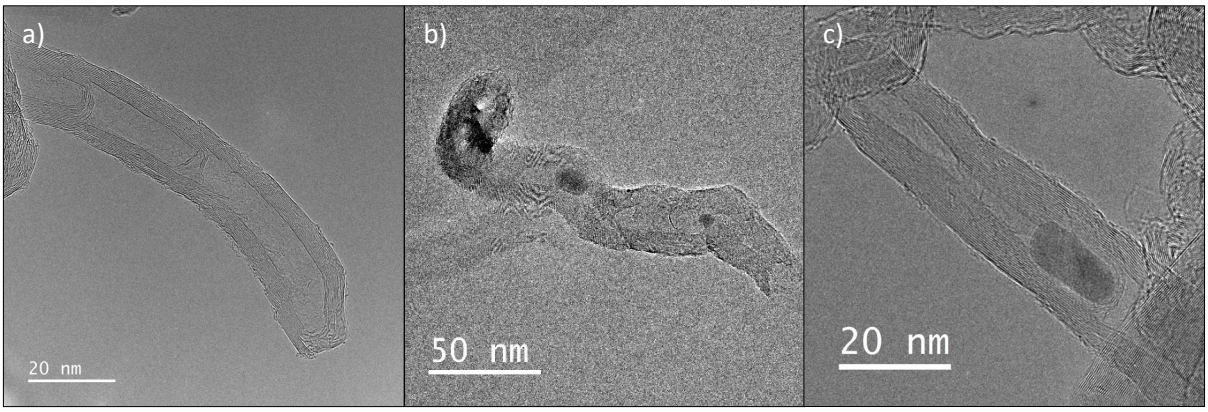

Fig. 17. Multi-walled CNTs of 10-30 graphene sheets from samples post Ni/YSZ and post-alkali Ni/YSZ, showing caps within a CNT (a), multiple Ni particles within a CNT (b), and one Ni particle encapsulated in the middle of a CNT (c).

5.1.4 | Amorphous and Turbostratic Carbon

Amorphous and turbostratic carbon can grow on both the Ni and YSZ particles. They are most noticeable at the edges of single particles where lattice fringes are visible, making the disordered carbon structures easier to distinguish. Fig. 18 shows the difference of a particle with and without amorphous carbon. Although identifying Ni particles among the YSZ particles is challenging, the amorphous/turbostratic growth undoubtedly covers both YSZ and Ni particles, as the Ni particles are distributed over the sample.

Both samples post Ni/YSZ and post-alkali Ni/YSZ show signs of amorphous/turbostratic carbon growing on the particles, and turbostratic carbon is also noticeable on many of the CNT structures, intertwined with the graphene sheet, see Fig. 19. As previously mentioned, there is a higher abundance of CNTs on the post Ni/YSZ compared to the post-alkali Ni/YSZ. However, it is not possible to state from the TEM images alone if there is more carbon/turbostratic growth on either sample, as these structures are more challenging to spot, and consequently, quantify.

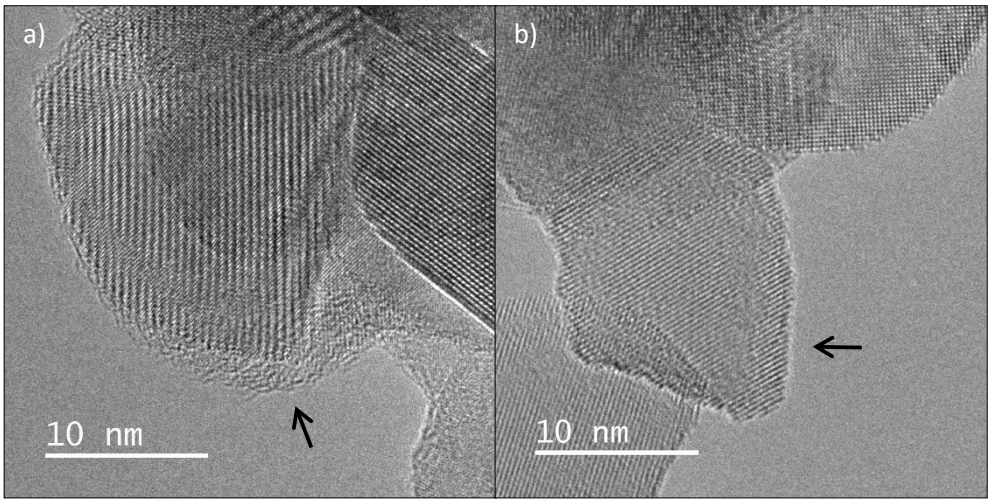

Fig. 18. Amorphous carbon growth on a single crystalline YSZ particle (see arrow) (a). A single crystalline YSZ particle without amorphous carbon growth (see arrow) (b).

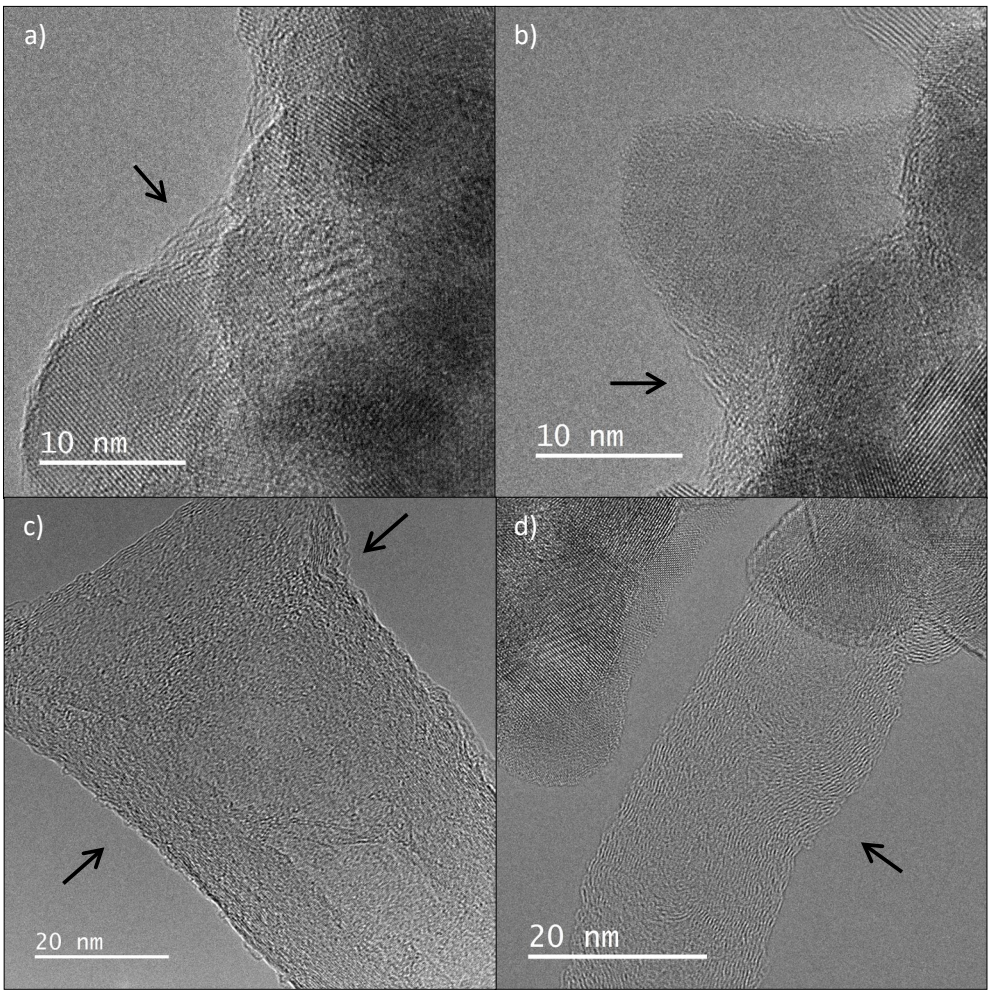

Fig. 19. Amorphous carbon on post samples: post Ni/YSZ and post-alkali Ni/YSZ, appearing on particles (a-b) and CNTs (c), and turbostratic carbon on CNTs (d). The carbon structures are highlighted with arrows.

5.1.5 | Carbon Whiskers

Carbon whiskers are observed growing on the CNTs on both post samples: post Ni/YSZ and post-alkali Ni/YSZ, see Fig. 20. The carbon whiskers can be distinguished from the CNTs where the graphene sheets grow at an inclined angle compared to the CNT growth axis, unlike the typical and more abundant CNTs where the graphene sheets grow parallel to the CNT growth axis. It was more challenging to find carbon whiskers in both samples, however, given that carbon whiskers grow on the CNTs, and given that the post-alkali Ni/YSZ sample had fewer CNTs compared to the post Ni/YSZ sample, it would be reasonable to assume that there are less carbon whiskers in the post-alkali Ni/YSZ sample.

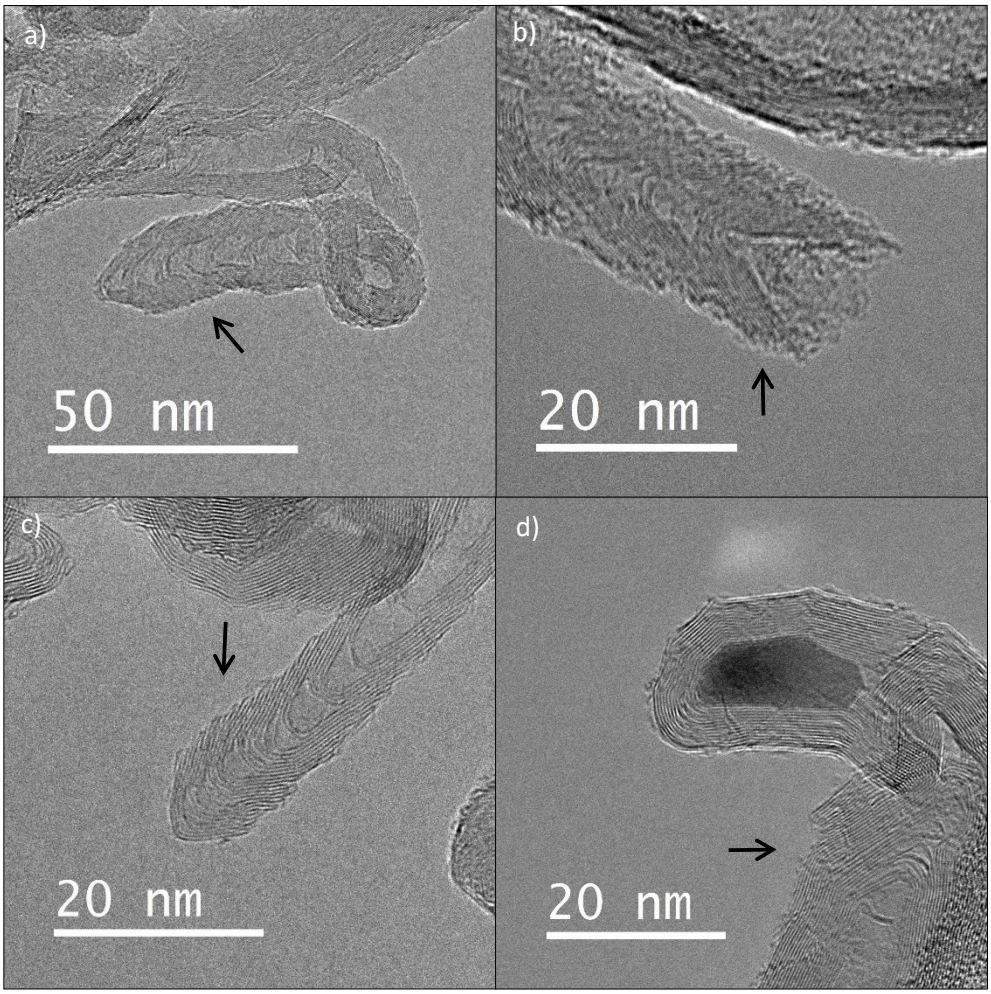

Fig. 20. Carbon whisker growth on (a-b) post Ni/YSZ and post-alkali Ni/YSZ (c-d). The graphene sheets grow at an inclined angle compared to the CNT growth axis. The arrows indicate the location of the carbon whiskers.

5.1.6 | Catalysts – Ni Nanoparticles

After the DRM reaction, the Ni particles either remain attached to the YSZ support or have detached from it if encapsulated in CNT growth due to coking. The quantity of Ni particles that were encapsulated could not be determined through the TEM images, however, once again, given the notable reduction in coking observed in the post-alkali Ni/YSZ compared to post Ni/YSZ, it is highly probably that these Ni particles underwent less coking in the post-alkali Ni/YSZ.

The presence of Ni, NiO and Ni_3C in the samples was confirmed through analysis using the FFT function in the GMS software. This involved manually selecting a Ni particle and applying FFT. Interplanar distances and angles between sets of spots from the FFT image were manually measured and compared to standard crystallographic data obtained from Single Crystal software matching Ni, NiO and Ni_3C, see an example of this from Fig. A1 in the Appendix. The lattice fringes of the Ni particles needed to be resolved in order to obtain the spots in the FFT, and therefore high-resolution images from the Titan E-cell 80-300ST TEM, with a spatial resolution of 0.8 Å, were used for analysing the Ni particles.

Locating Ni particles on YSZ is generally difficult, due to multiple spots appearing in the FFT when applied to areas with numerous overlapping crystalline particles from both Ni and YSZ,

making interpretation difficult. This compared to analysing Ni particles within the CNTs, where it is already known that these particles are Ni. Fig. 21 shows three particles that were found to be Ni, NiO and Ni_3C, and their corresponding FFT. Table 3 shows the measured interplanar distances and angles between the spots, that were compared to crystallographic data of Ni, NiO and Ni_3C from Single Crystal.

Only a few of all the Ni particles measured could be distinguished as either Ni, NiO or Ni_3C, and it was not possible to draw any conclusion due to insufficient data. However, of the few measured particles, the encapsulated Ni particles appear to be either Ni or Ni_3C and the non-encapsulated ones to NiO. This aligns with Ni particles oxidising to NiO when exposed to air post reaction, or even during reaction by oxygen atoms, while encapsulated Ni particles remain pure Ni metal or transform into Ni_3C by reacting with carbon atoms from the CNTs.

Table 3. Three Ni particles corresponding to Ni, NiO and Ni_3C. Interplanar distances measured from the spots of the FFT images, Fig. 21, and compared to spots from Single Crystal (SC) data matching particles Ni, NiO or Ni_3C. The measured angles between the spots corresponding to interplanar distances (x/y)Å, match the angles obtained between spots from the SC data for Ni, NiO and Ni_3C.

Crystallographic orientation	**Measured Ni particle**	**Ni_3C (SC)**	**NiO (SC)**	**Ni (SC)**
a) (110)	**54.2°** (2.118/2.515)Å **53.5°** (2.118/2.506)Å **72.3°** (2.515/2.506)Å	-	**55.0°** (2.089/2.412)Å (002)-(-111) **55.0°** (2.089/2.412)Å (002)-(1-11) **70.0°** (2.412/2.412)Å (-111)-(1-11)	-
b) (110)	**71.3°** (1.777-1.061)Å **74.8°** (1.777-1.059)Å **34.0°** (1.061-1.059)Å	**73.5°** (1.898/1.089)Å (2-20-2)-(2-2010) **73.5°** (1.898/1.085)Å (2-20-2)-(000 12) **33.0°** (1.089/1.085)Å (2-20-2)-(2-2010)	-	-
c) (110)	**69.7°** (2.132-2.012)Å **57.5°** (2.132-1.832)Å **53.1°** (2.012-1.832)Å	-	-	**70.0°** (2.046/2.046)Å (1-11)-(1-1-1) **55.0°** (2.046/1.772)Å (1-11)(002) **55.0°** (2.046/1.772)Å (1-1-1)-(00-2)

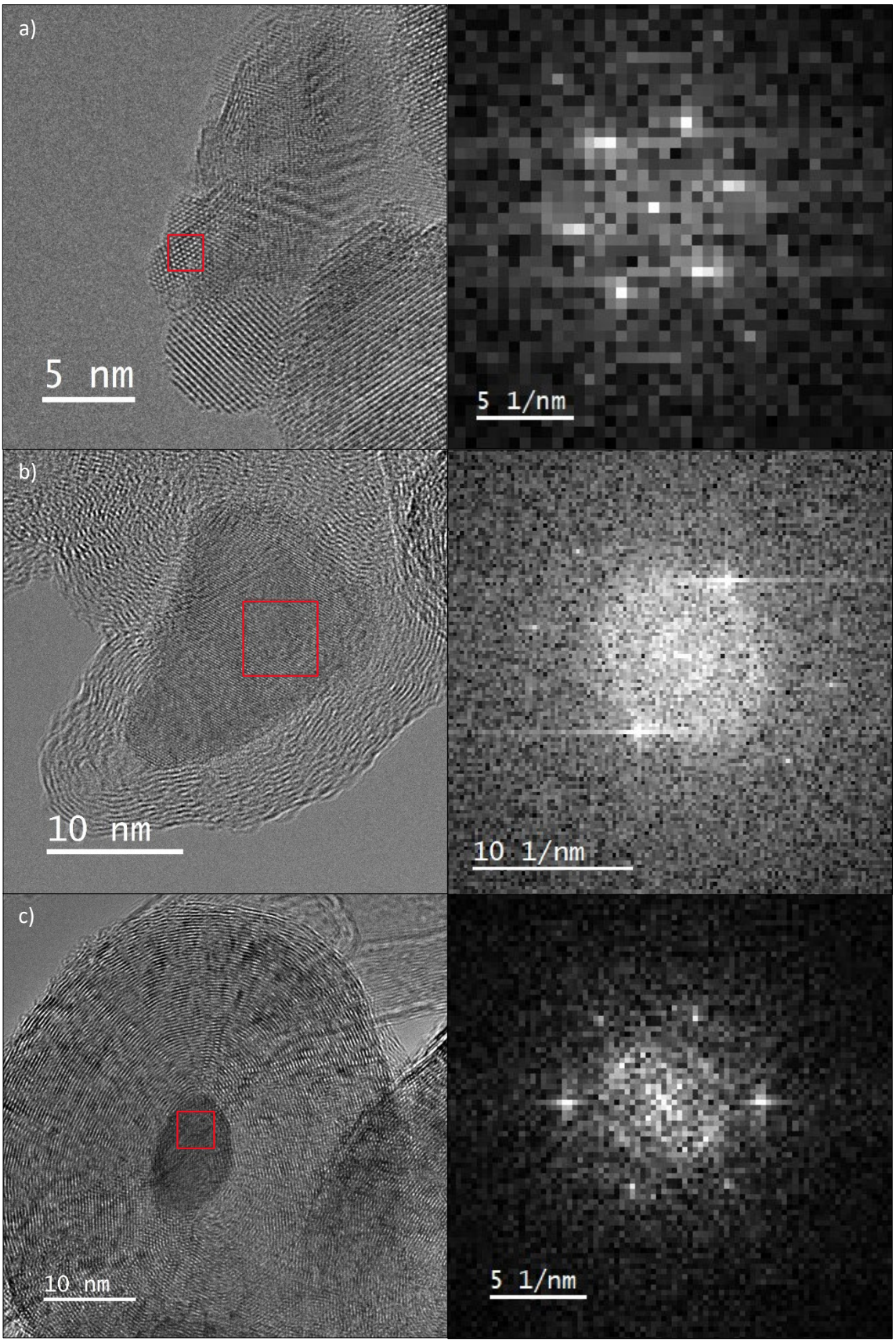

Fig. 21. Three Ni particles NiO (a), Ni_3C (b), Ni (c), post DRM reaction with corresponding FFT.

5.2 | STEM-XEDS Mapping – Analysis of Sintering

To examine whether sintering had occurred post DRM reaction and determine if there were difference between the post Ni/YSZ and post-alkali Ni/YSZ, STEM-XEDS was performed on the Titan E-cell 80-300ST TEM. Data collected from different sites of the samples were processed by the software AZtec, where each scanned site was converted into a map displaying the Ni particle distribution. These maps were further analysed in the software GMS, where the Ni particle sizes were manually measured.

5.2.1 | Sintering pre DRM Reaction – with and without Promoters

The STEM-XEDS maps of the pre Ni/YSZ and pre-alkali Ni/YSZ are displayed in Fig. 22. The Ni particles are distributed across the sample, and larger well-defined particles have not formed. This is anticipated for the pre DRM reaction, as significant level of sintering is not expected to have occurred at this stage. The Ni particle sizes were measured from several sites, and an average size of <4.5 nm with a standard deviation (SD) of 2.4 nm was found for pre Ni/YSZ, and <10.1 nm with a SD of 4.1 nm for pre-alkali Ni/YSZ, see Table 4. The symbol "<" is used to denote that only the larger and somewhat more defined particles have been measured, excluding smaller particles that were difficult to distinguish from noise. Therefore, determining whether the particles in the pre-alkali Ni/YSZ are larger than those in the pre Ni/YSZ is not straightforward, given the marginal difference of only 5.6 nm. If the particles in the pre-alkali sample are indeed slightly larger, a possible explanation could be that the alkali promoters might promote diffusion and/or alter the surface energy of the Ni particles further facilitating sintering, even pre reaction. Another possibility is that the alkali promoters could modify the surface chemistry of the Ni particles, increasing their reactivity when colliding.

Table 4. Ni particle measurements for pre and post DRM reaction. Standard deviation is indicated by SD, #sites and #particles indicate how many sites were examined and the total amount of Ni particles measured from these sites.

	Average Ni particle size (nm)	**#sites**	**#particles**	**SD (nm)**
Pre Ni/YSZ	<4.5	6	98	2.4
Pre-alkali Ni/YSZ	<10.1	11	364	4.1
Post Ni/YSZ	21.8	11	134	6.1
Post-alkali Ni/YSZ	18.8	10	87	6.7

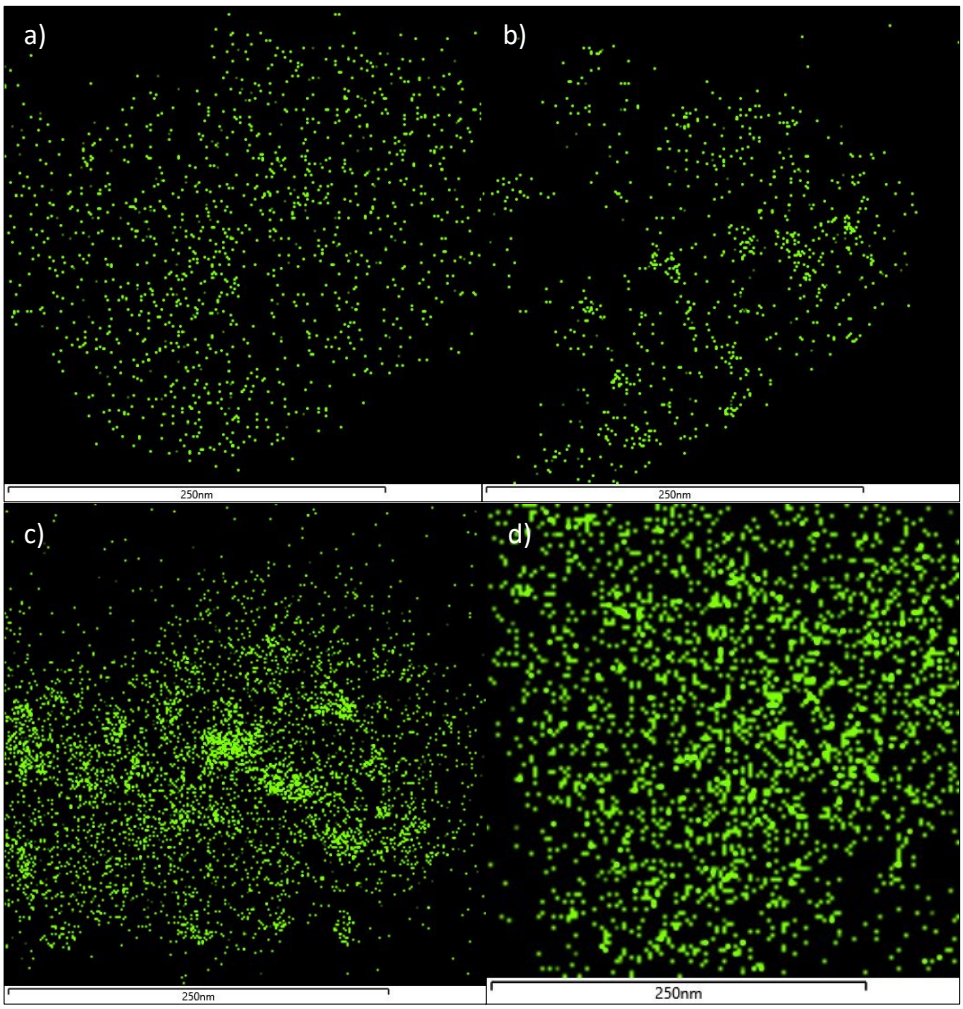

Fig. 22. STEM-XEDS maps showing the distribution of Ni catalyst particles for samples: pre Ni/YSZ (a-b) pre-alkali Ni/YSZ and (c-d).

5.2.2 | Sintering post DRM Reaction – with and without Promoters

HAADF images and STEM-XEDS maps of the post Ni/YSZ and post-alkali Ni/YSZ are displayed in Fig. 23. These particles are larger in size, more well-defined, and less distributed across the sample compared to the pre reaction samples, indicating that particle sintering has occurred. The Ni particles were measured from several sites, and an average size of 21.8 nm, with a SD of 6.1 nm was found for the post Ni/YSZ, and 18.8 nm with a SD of 6.7 nm for the post-alkali Ni/YSZ, see Table 4.

Initially 128x128 pixel images were captured for measuring Ni particles. However, due to difficulties in distinguishing boundaries of each particle, more detailed images at 256x256 pixels were recorded for comparison. STEM scanning over 256x256 pixels is significantly more time-consuming and is only worth considering if the results are substantially different. Comparing a 128x128 pixel and a 256x236 pixel image from the same site, taken from post-alkali Ni/YSZ, it was observed that the Ni particles from the 128x128 were measured as larger particles, or as a single larger particle instead of two adjacent smaller particles, compared to the 256x256. Thus, new data from 256x256 pixel images was provided by Professor Thomas Willum Hansen, DTU, using the new microscope Thermo-Fischer Spectra Ultra, see Fig. 23(c)**.** The average particle size of 544 Ni particles taken from 9 sites from the post-alkali Ni/YSZ was

measured to be 18.8 nm with a SD of 7.1 nm, matching the measurement of 18.8 nm from 128x128 pixel images taken from the same sample. This suggested that even though small errors may occur by manual measuring individual particles, the resulting average particle size is not affected.

It is apparent that there is not a significant difference between the average particle size for post Ni/YSZ and post-alkali Ni/SZ, 21.8 nm and 18.8 nm. This suggest that sintering occurs to a similar degree regardless of the presence of alkali promoters under these DRM reaction conditions.

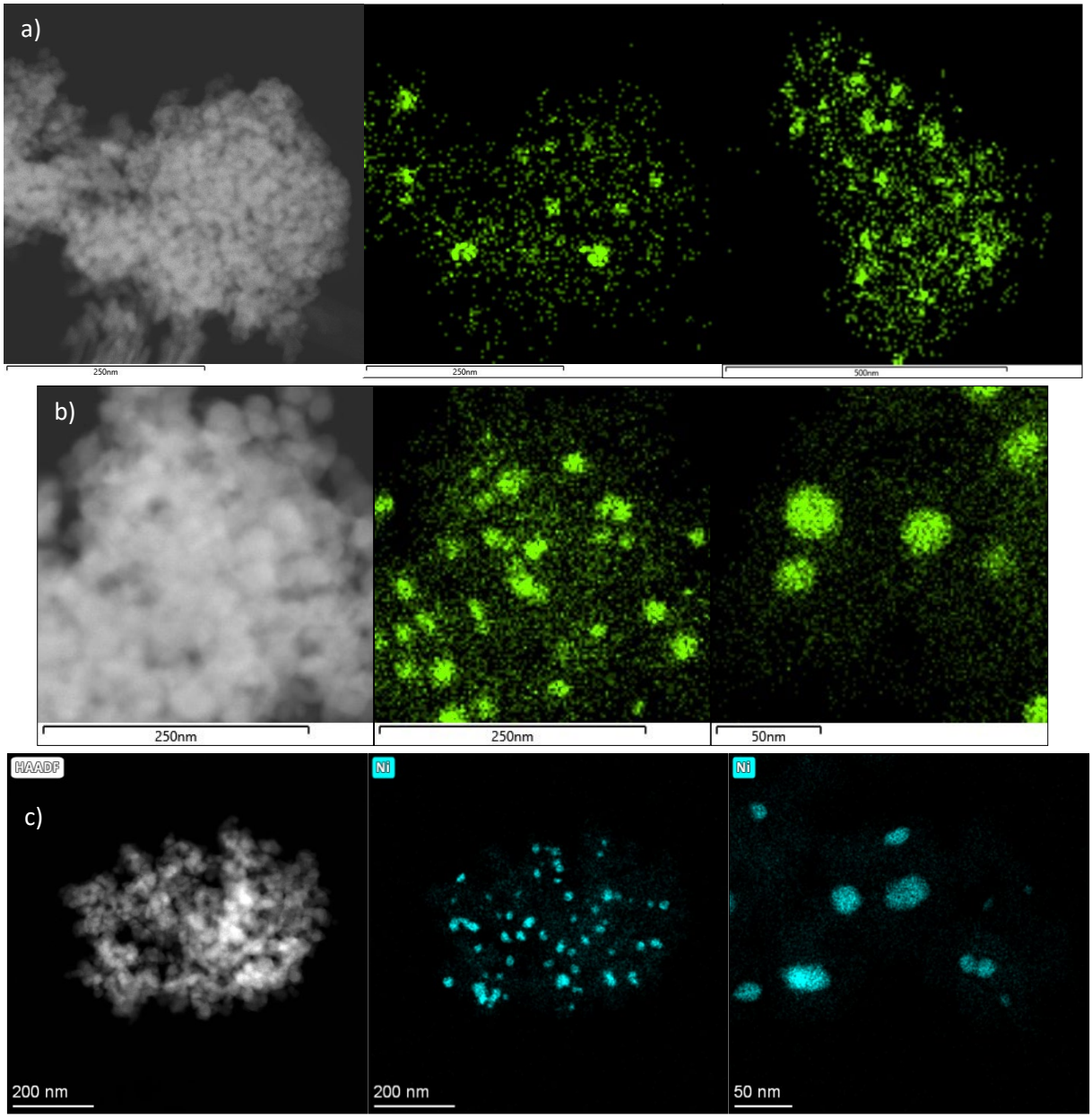

Fig. 23. HAADF images (left images) and corresponding STEM-XEDS maps (middle images), and additional STEM-XEDS maps (right images) showing the distribution of Ni catalyst particles from samples: post Ni/YSZ, captured at 128x128 pixels (a), post-alkali Ni/YSZ, 128x128 pixels (b) and post-alkali Ni/YSZ, 256x256 pixels (c).

5.2.3 | Ni Catalyst Activity and TPO Measurements

To obtain a quantitative representation of the various carbon structures resulting from coking, from the post Ni/YSZ and post-alkali Ni/YSZ samples, TPO was performed. Furthermore, Ni catalyst activity measurements were performed to find a correlation between catalyst deactivation with respect to coking and sintering, observed in the TEM images, XEDS-STEM maps and TPO data. The data of the TPO and the catalyst activity measurements were provided by Professor Søren Kegnæs and his team, DTU.

5.2.3.1 | TPO Measurements

The TPO measurements are shown in Fig. 24. The post Ni/YSZ (red plot) exhibits significantly more coking compared to the post-alkali Ni/YSZ (green plot). The temperature range for carbon oxidation of the post Ni/YSZ extends from approximately 320-670°C, with two distinct peaks observed around 420°C and 600°C. Amorphous carbon is more reactive than crystalline graphene carbon due to its larger surface area and lower thermodynamic stability, resulting from its high degree of structural disorder. Consequently, it begins to oxidise at a lower temperature compared to crystalline graphene carbon. Correlating the TPO measurements with the various carbon structures observed in the TEM images: amorphous, turbostratic and graphene (CNTs), the peak at 420°C likely corresponds to amorphous carbon oxidation, while the peak at 600°C likely corresponds to crystalline graphene oxidation (CNTs). The transition area between the peaks is most probably a mixture of amorphous and graphene oxidation, along with oxidation of turbostratic carbon, exhibiting both amorphous and crystalline characteristic.

For the post-alkali Ni/YSZ, the temperature range for carbon oxidation range from 340-560°C, with a peak observed around 420°C, aligning with the 420°C peak from post Ni/YSZ, and likely to correspond to oxidation of amorphous carbon. The post-alkali Ni/YSZ peak is estimated to be approximately 15% of the peak for post Ni/YSZ, suggesting a significantly lower presence of amorphous carbon. This distinction could not be made based solely on the TEM images. It was however evident that there was significant less CNTs in the post-alkali Ni/YSZ based of the TEM data. There is no visible peak around 600°C, however, there is a small area between 500-560°C, and it is possible it corresponds to turbostratic carbon and crystalline graphene (CNTs).

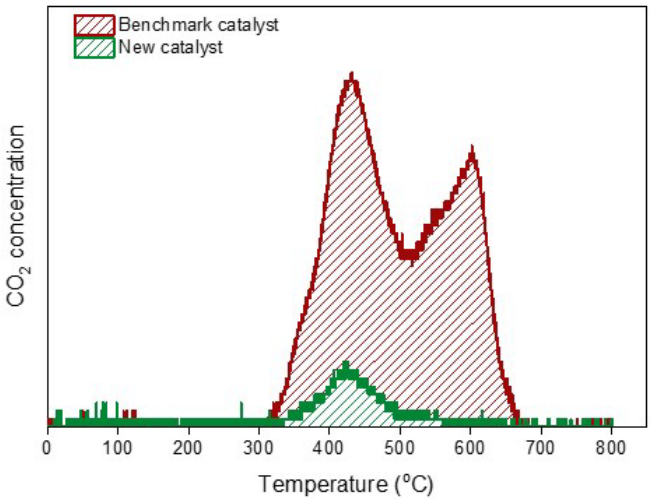

Fig. 24. TPO measurements of samples post Ni/YSZ (red plot) and post-alkali Ni/YSZ (green plot). Post-alkali Ni/YSZ exhibits less coking compared to post Ni/YSZ.

5.2.3.2 | Ni Catalyst Activity Measurements

The activity of the Ni particles during the DRM reaction can be seen in Fig. 25. The post Ni/YSZ (red plot) showed a decrease in CO_2 conversion of approximately 20% over 50 hours while the post-alkali Ni/YSZ (green plot) showed a decrease of approximately 10% over the same duration. This indicates a loss in catalytic activity of 20% for post Ni/YSZ and 10% for post-alkali Ni/YSZ.

In the case of post-alkali Ni/YSZ, the decline is more prominent during the initial phase of the reaction, particularly the 5-10 hours, after which it gradually levels off over the course of 50 hours. Similarly, the decline is more prominent during the initial phase for the post Ni/YSZ, however, it continues to decline at a slower rate. These findings underscore the promotive effects that the alkali promoters have on the DRM reaction. Based on the data from XEDS-STEM maps, sintering is occurring at comparable extent in both samples. Furthermore, observations from TEM imaging and TPO measurements indicate that coking is mainly observed on the post Ni/YSZ sample.

Considering these findings in relation to the Ni catalyst activity measurements, it suggests that the rapid decline in CO_2 conversion during the initial phase of the DRM reaction is likely attributed to both sintering and coking observed in both samples. As sintering ceases, the decline in CO_2 conversion slows down, and only coking continues to affect the conversion rate. This ceasing in sintering may be due to as larger particles begin to form due to sintering, eventually the energy needed to overcome repulsive forces between two particles exceeds the energy gained by the reduction in surface area from particle formation, and at some point, the particles stop growing. Another explanation could be that over time, as smaller particles merge into larger particles, from both PMC and OR, there are fewer and less distributed particles compared to the initial well distributed phase, resulting in a higher particle diffusion barrier that slows down the sintering process.

Given that coking can occur throughout the reaction and is predominantly observed in the post Ni/YSZ, it likely contributes to the more pronounced decline in catalyst activity observed over the entire 50-hour period compared to the post-alkali Ni/YSZ. Hence, it appears that the alkali promoters added to post-alkali Ni/YSZ, enhance the activity of the Ni catalysts by reducing coking, leading to an increase in production yield of the DRM reaction. However, the alkali promoters do not appear to affect the sintering process.

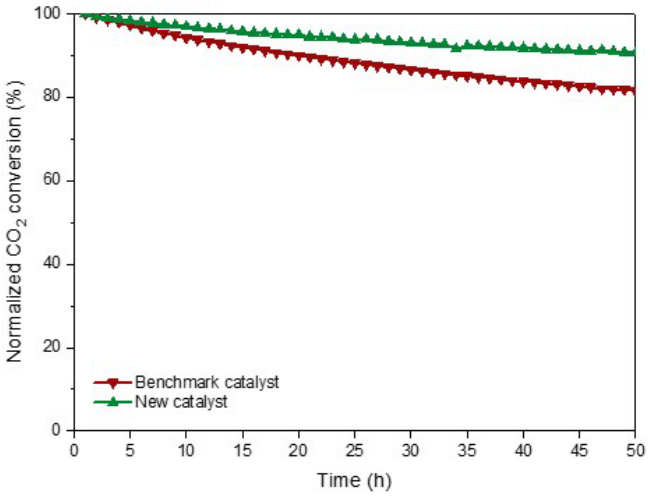

Fig. 25. Ni catalyst activity measurements of samples post Ni/YSZ (red plot) and post-alkali Ni/YSZ (green plot). Post-alkali Ni/YSZ exhibits higher catalyst activity compared to post Ni/YSZ.

6 | Conclusion

In this thesis, the impact of added alkali promoters on Ni catalysts supported on YSZ (post-alkali Ni/YSZ) was examined to evaluate their effect on catalytic activity in DRM, compared to the unpromoted sample (post Ni/YSZ). Coking and sintering causing loss in catalyst activity, were analysed using a range of techniques, including TEM imaging for analysing coking, STEM-XEDS for analysing sintering, TPO for examining coking levels, and catalytic activity measurements for evaluating overall catalytic performance.

Analysis of coking through TEM imaging and TPO measurements revealed the presence of various forms of coking, including amorphous, turbostratic and graphene carbon (CNTs) on both post reaction samples. Post-alkali Ni/YSZ showed significantly less carbon growth, suggesting that the added alkali promoters effectively reduced coking. This reduction in coking translates to fewer catalytic active sites being blocked by carbon growth, thereby reducing the loss of catalyst activity. Analysis of Ni catalyst particle size distribution using STEM-XEDS revealed comparable levels of sintering between the post reaction samples. The average Ni particle size increased from <4.5 nm pre Ni/YSSZ to 21.8 nm post Ni/YSZ, and from <10.1 nm pre-alkali Ni/YSZ to 18.8 nm post-alkali Ni/YSZ. The difference in average particle size between post reaction samples was only 3.0 nm, indicating minimal variation in sintering. Furthermore, catalytic activity measurements based on the CO_2 conversion percentage showed a 10% loss in catalyst activity for post-alkali compared to 20% loss in catalyst activity for post Ni/YSZ over a 50-hour reaction period, showing enhanced catalytic activity for post-alkali Ni/YSZ.

In conclusion, the addition of alkali promoters to Ni catalysts supported on YSZ led to improved catalytic activity compared to the unpromoted sample, owing to significantly less coking. The alkali promoters did not suppress sintering.

7 | References

[1] Y. Song *et al.*, “Dry reforming of methane by stable Ni–Mo nanocatalysts on single-crystalline MgO,” *Science*, vol. 367, no. 6479, pp. 777–781, Feb. 2020, doi: https://doi.org/10.1126/science.aav2412.

[2] W.-C. Chung and M.-B. Chang, “Review of catalysis and plasma performance on dry reforming of CH4 and possible synergistic effects,” *Renewable and Sustainable Energy Reviews*, vol. 62, pp. 13–31, Sep. 2016, doi: https://doi.org/10.1016/j.rser.2016.04.007.

[3] Z. Alipour, M. Rezaei, and Fereshteh Meshkani, “Effect of alkaline earth promoters (MgO, CaO, and BaO) on the activity and coke formation of Ni catalysts supported on nanocrystalline Al2O3 in dry reforming of methane,” *Journal of Industrial and Engineering Chemistry*, vol. 20, no. 5, pp. 2858–2863, Sep. 2014, doi: https://doi.org/10.1016/j.jiec.2013.11.018.

[4] J. Sehested, “Four challenges for nickel steam-reforming catalysts,” *Catalysis Today*, vol. 111, no. 1–2, pp. 103–110, Jan. 2006, doi: https://doi.org/10.1016/j.cattod.2005.10.002.

[5] Y. Zhang *et al.*, “Dry reforming of methane over Ni/SiO2 catalysts: Role of support structure properties,” *Fuel*, vol. 340, p. 127490, May 2023, doi: https://doi.org/10.1016/j.fuel.2023.127490.

[6] J. Zhang and F. Li, “Coke-resistant Ni@SiO2 catalyst for dry reforming of methane,” *Applied Catalysis B: Environmental*, vol. 176–177, pp. 513–521, Oct. 2015, doi: https://doi.org/10.1016/j.apcatb.2015.04.039.

[7] H. Seo, “Recent Scientific Progress on Developing Supported Ni Catalysts for Dry (CO2) Reforming of Methane,” *Catalysts*, vol. 8, no. 3, p. 110, Mar. 2018, doi: https://doi.org/10.3390/catal8030110.

[8] A. G. S. Hussien and K. Polychronopoulou, “A Review on the Different Aspects and Challenges of the Dry Reforming of Methane (DRM) Reaction,” *Nanomaterials*, vol. 12, no. 19, p. 3400, Sep. 2022, doi: https://doi.org/10.3390/nano12193400.

[9] J.-M. Lavoie, “Review on dry reforming of methane, a potentially more environmentally-friendly approach to the increasing natural gas exploitation,” *Frontiers in Chemistry*, vol. 2, Nov. 2014, doi: https://doi.org/10.3389/fchem.2014.00081.

[10] C. H. Bartholomew, “Mechanisms of catalyst deactivation,” *Applied Catalysis A: General*, vol. 212, no. 1–2, pp. 17–60, Apr. 2001, doi: https://doi.org/10.1016/s0926-860x(00)00843-7.

[11] A. T. DeLaRiva, T. W. Hansen, S. R. Challa, and A. K. Datye, “ChemInform Abstract: In situ Transmission Electron Microscopy of Catalyst Sintering,” *ChemInform*, vol. 45, no. 3, p. no-no, Jan. 2014, doi: https://doi.org/10.1002/chin.201403260.

[12] T. W. Hansen, A. T. DeLaRiva, S. R. Challa, and A. K. Datye, “Sintering of Catalytic Nanoparticles: Particle Migration or Ostwald Ripening?,” *Accounts of Chemical Research*, vol. 46, no. 8, pp. 1720–1730, May 2013, doi: https://doi.org/10.1021/ar3002427.

[13] Y. W. Budhi *et al.*, “Enhancing the catalytic performance and coke reduction using low-cost Ni-based promoted catalyst for hydrogen production,” *Journal of Industrial and Engineering Chemistry*, Aug. 2023, doi: https://doi.org/10.1016/j.jiec.2023.08.013.

[14] J. C. Acomb, C. Wu, and P. T. Williams, “Effect of growth temperature and feedstock:catalyst ratio on the production of carbon nanotubes and hydrogen from the pyrolysis of waste plastics,” *Journal of Analytical and Applied Pyrolysis*, vol. 113, pp. 231–238, May 2015, doi: https://doi.org/10.1016/j.jaap.2015.01.012.

[15] S. Andreoli and S. Eser, “Relating reactivity to structure in cokes and carbon materials: Temperature-programmed oxidation and microscopy techniques,” *Carbon*, vol. 168, pp. 362–371, Oct. 2020, doi: https://doi.org/10.1016/j.carbon.2020.06.071.

[16] S. Helveg *et al.*, “Atomic-scale imaging of carbon nanofibre growth,” *Nature*, vol. 427, no. 6973, pp. 426–429, Jan. 2004, doi: https://doi.org/10.1038/nature02278.

[17] C. F. Escalante and S. Escalante , “Fundamentals of transmission electron microscopy, the technique with the best resolution in the world,” Feb. 2019.

[18] C Barry Carter and D. B. Williams, *Transmission Electron Microscopy Diffraction, Imaging, and Spectrometry*. Cham Springer International Publishing, 2016.

[19] J. Liu, “Scanning transmission electron microscopy and its application to the study of nanoparticles and nanoparticle systems,” *Microscopy*, vol. 54, no. 3, pp. 251–278, Jun. 2005, doi: https://doi.org/10.1093/jmicro/dfi034.

[20] S. Li *et al.*, “Tuning strong metal-support interactions to boost activity and stability of aluminium nitride supported nickel catalysts for dry reforming of methane,” *Fuel*, vol. 343, p. 127918, Jul. 2023, doi: https://doi.org/10.1016/j.fuel.20

[21]“Welcome to the Laboratory of Laser Photochemistry! | LLP,” *llp.inflpr.ro*. https://llp.inflpr.ro/

[22] Y. Liu *et al.*, “Significantly enhanced critical current density in nano-MgB_2grains rapidly formed at low temperature with homogeneous carbon doping,” *Superconductor science and technology/Superconductor science & technology*, vol. 28, no. 5, pp. 055005–055005, Mar. 2015, doi: https://doi.org/10.1088/0953-2048/28/5/055005.

[23] Crina Ghemes, “Synthesis of Long and Spinnable Multi-Walled Carbon Nanotubes,” vol. 3, no. 1, Jun. 2012.

[24] S. Helveg, J. Sehested, and J. R. Rostrup-Nielsen, “Whisker carbon in perspective,” *Catalysis Today*, vol. 178, no. 1, pp. 42–46, Dec. 2011, doi: https://doi.org/10.1016/j.cattod.2011.06.023.

[25] A. Verma, R. Arif, and Sapana Jadoun, “Synthesis, Characterization, and Application of Modified Textile Nanomaterials,” pp. 167–187, Mar. 2020, doi: https://doi.org/10.1002/9781119620396.ch8.

[26] M. N. Tsampas, F. M. Sapountzi, and P. Vernoux, “Applications of yttria stabilized zirconia (YSZ) in catalysis,” *Catalysis Science & Technology*, vol. 5, no. 11, pp. 4884–4900, Oct. 2015, doi: https://doi.org/10.1039/C5CY00739A.

[27] M. Cichy and W. Zawadzki, “The influence of alkaline promoters on the properties of the Ni/HAp catalyst in the methane dry reforming reaction,” *Physicochemical Problems of Mineral Processing*, Jan. 2024, doi: https://doi.org/10.37190/ppmp/182856.

[28] X. Gao, J. Ashok, and S. Kawi, “Smart Designs of Anti-Coking and Anti-Sintering Ni-Based Catalysts for Dry Reforming of Methane: A Recent Review,” *Reactions*, vol. 1, no. 2, pp. 162–194, Dec. 2020, doi: https://doi.org/10.3390/reactions1020013.

[29] “DoITPoMS - TLP Library Fuel Cells,” *www.doitpoms.ac.uk*. https://www.doitpoms.ac.uk/tlplib/fuel-cells/printall.php

[30] “Scanning Transmission Electron Microscopy - Nanoscience Instruments.” https://www.nanoscience.com/techniques/scanning-transmission-electron-microscopy/

[31] “Virtual Labs,” *emb-iitk.vlabs.ac.in*. https://emb-iitk.vlabs.ac.in/exp/field-imaging/theory.html

Appendix

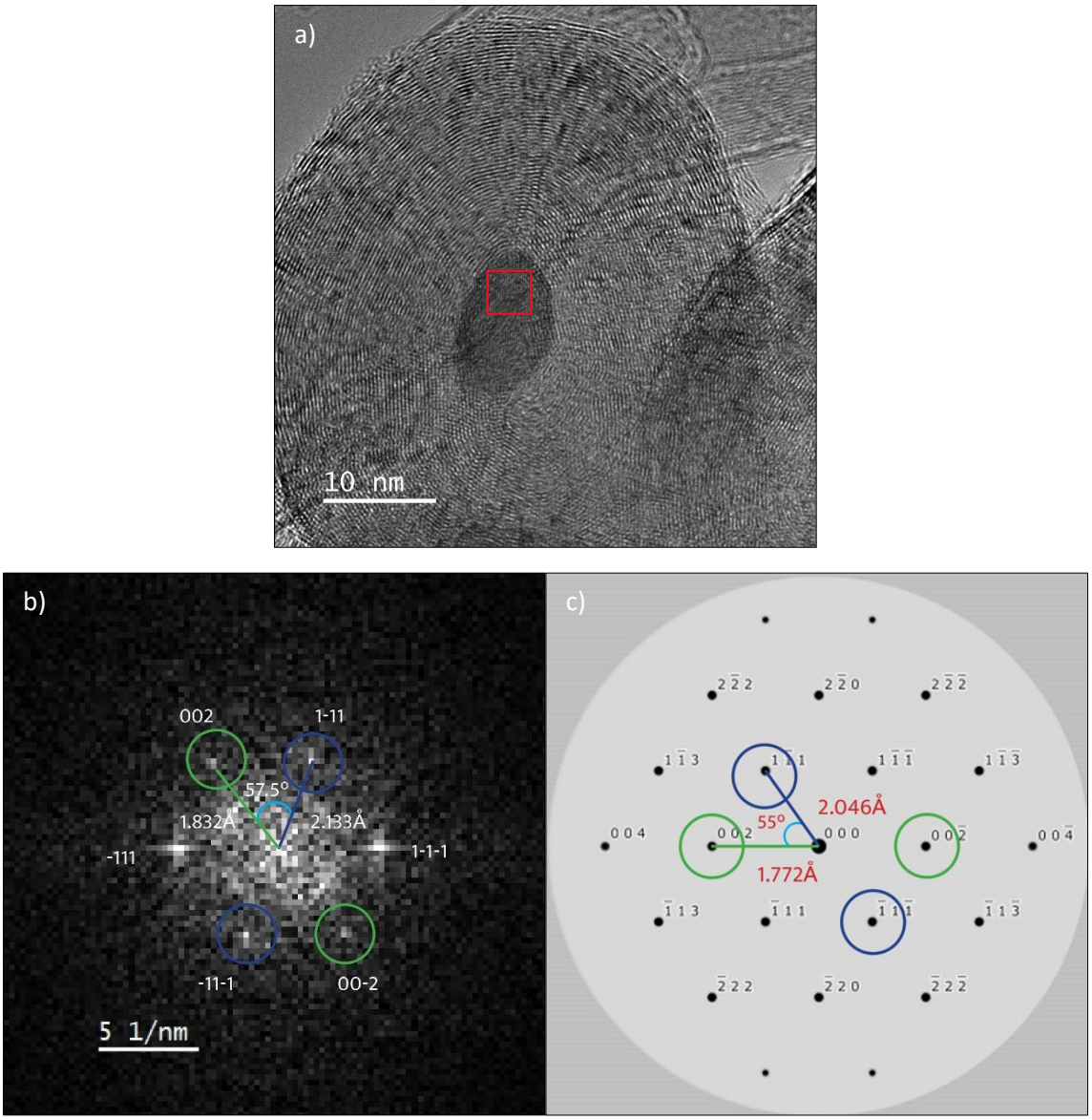

Fig. A1. TEM image of an encapsulated Ni particle (a) with corresponding FFT of the rectangular area containing only the Ni particle (b). Matching the spots from the FFT image (b) to crystallographic data from Single Crystal (c) by comparing measured angles and interplanar distances between the sets of spots. Further data is provided in Table 3(c). The measured Ni particle matches to pure Ni, with the crystallographic orientation (100), Ni(100). This example shows the comparison of 2 sets of spots, however at least 3 sets of spots were required for comparison to be able to rule out NiO and Ni_3C.